Stefan Pereira do Ó

Licenciado em Ciências de Engenharia Mecânica

Wire and Arc Additive Manufacturing: Developments and Parts Characterization

Dissertação para obtenção do Grau de Mestre em

Engenharia Mecânica

Orientador: Professor Doutor Telmo Jorge Gomes dos Santos, Professor Associado com Agregação, Faculdade de Ciências e Tecnologia da Universidade Nova de Lisboa

Coorientador: Professor Doutor João Pedro de Sousa Oliveira, Professor Auxiliar, Faculdade de Ciências e Tecnologia da Universidade Nova de Lisboa

Júri:

Presidente: Prof. Doutora Carla Maria Moreira Machado

Arguente: Prof. Doutora Catarina Isabel Silva Vidal

Vogal: Prof. Doutor Telmo Jorge Gomes dos Santos

FACULDADE DE CIÊNCIAS E TECNOLOGIA
UNIVERSIDADE NOVA DE LISBOA

Setembro 2019

Wire and arc additive manufacturing: developments and parts characterization

To my family

Acknowledgments

First, I would like to express my gratitude to my supervisor Professor Telmo Santos for his knowledge, continuous support and guidance throughout this work.

Second, to my co-supervisor, Professor João Oliveira who always made himself available when I needed help.

I am also deeply thankful to Valdemar Duarte and Tiago Rodrigues for their constant help, support and friendship over the last 7 months.

To Mr. António Campos and Mr. Paulo Magalhães for their essential help, everyday assistance and good humor.

To Francisco Ferreira for all the time spent helping me in CENIMAT.

To Patrick Inácio for the help setting up the thermocouple measurement circuit.

To Miguel Machado for helping me with the plastic 3D printer every time difficulties were encountered.

To all my laboratory colleagues who were always ready to help, and contributed to making the workspace an enjoyable place filled with good ideas, humor and a sense of companionship.

I am also very grateful for the support received from my closest friends.

A special thanks goes to my girlfriend for her patience and support throughout these stressful times.

Finally, I would like to thank my mother and my grandparents for making this all possible having always provided me with everything, including my education and for their support during this journey, thank you!

Resumo

Wire and arc additive manufacturing (WAAM) é uma tecnologia que requer pouco investimento e permite uma redução nos materiais utilizados assim como no tempo de produção, ao mesmo tempo que possibilita a produção de peças complexas. Mas apesar das suas vantagens, componentes produzidos através desta técnica estão sujeitos a defeitos dependendo dos materiais usados e em regra apresentam propriedades mecânicas inferiores quando comparados com processos convencionais.

Este trabalho teve como objectivo construir e testar um sistema capaz de controlar os ciclos térmicos durante o processo de WAAM, de modo a controlar as taxas de arrefecimento, e consequentemente a microestrutura das peças produzidas, a fim de controlar a dureza das mesmas.

Dois permutadores foram construídos, um para aquecer e outro para arrefecer os gases de protecção. Os permutadores foram testados através da produção de paredes de aço inoxidável 316L e de Inconel 625, uma superliga de níquel. Foram feitas amostras utilizando gás quente, frio e a temperatura ambiente, e as mesmas foram caracterizadas quanto à sua geometria, dureza e microestrutura.

Conclui-se que variar a temperatura dos gases de protecção por si só não é suficiente para se produzir um efeito significativo na microestrutura e nas propriedades mecânicas das peças. Utilizando o sistema de frio com o arrefecimento ligado provocou um aumento na dureza de até 30 HV e uma redução de 13.2 % no tamanho das dendrites para as amostras realizadas com Inconel 625. Utilizando este mesmo sistema sem o arrefecimento ligado resultou num aumento de 16.8 % da largura efectiva e uma redução de 15.8 % da altura das paredes de aço inoxidável 316L. Estas diferenças deveram-se ao permutador utilizado para arrefecer servir de dissipador ou acumulador dependendo se o arrefecimento estava ligado ou desligado.

Palavras-chave

Manufactura aditiva, WAAM, soldadura por arco eléctrico, aço inoxidável 316L, superliga de níquel Inconel 625

Abstract

Wire and arc additive manufacturing (WAAM) is a low capital investment technology that allows a reduction in material usage and production times while enabling the production of complex components. But despite its advantages, components produced in WAAM are prone to defects depending on the materials used and have overall inferior mechanical properties when compared to conventional processes.

This study focused on building and testing a system capable controlling the thermal cycles to manipulate the cooling rates and consequently the microstructure of produced parts in order to control the resulting hardness.

Two heat exchangers were built, one to heat and the other to cool the shielding gases. The exchangers were tested through the manufacturing of thin walls of 316L stainless steel and Inconel 625 superalloy using hot, ambient and cold argon gas. Obtained parts where characterized for their geometry, hardness and microstructure.

It was shown that varying the temperature of the shielding gas by itself is not enough to significantly influence the microstructure and mechanical properties of WAAM components. Using the cooling heat exchanger with cooling turned on caused an increase in hardness up to 30 HV and a decrease in primary dendrite arm spacing (PDAS) of 13.2 % for Inconel 625 while using the same heat exchanger without cooling caused an increase of 16.8 % in effective wall width (EWW) and a decrease of 15.8 % in height for 316L stainless steel. These differences were due to the cooling exchanger acting as a heat sink or as a heat accumulator depending on whether the cooling was turned on or off.

Key-words

Additive Manufacturing, WAAM, arc welding, 316L stainless steel, Inconel 625 superalloy

Contents

List of figures

List of tables

Acronyms

3D	Three-Dimensional
AM	Additive Manufacturing
FZ	Fusion Zone
GFR	Gas Flow Rate [L min^{-1}]
GMAW	Gas Metal Arc Welding
HAZ	Heat Affected Zone
HI	Heat Input [J mm^{-1}]
HV	Hardness Vickers [HV]
I	Current Intensity [A]
MAG	Metal Active Gas
MIG	Metal Inert Gas
PDAS	Primary Dendrite Arm Spacing [μm]
TS	Travel Speed [mm s^{-1}]
U	Voltage [V]
WAAM	Wire and Arc Additive Manufacturing
WFS	Wire Feed Speed [m min^{-1}]

1 Introduction

1.1 Motivation

With an ever-growing need to reduce costs and optimize processes in order to compete within the industrial world, some conventional subtractive processes are being replaced by additive manufacturing (AM) processes. Wire and Arc Additive Manufacturing (WAAM) is an AM process that has proven to be a suitable solution by allowing a reduction in material usage and production times while enabling the production of complex components [1].

Despite its numerous advantages, there are still some challenges that need to be addressed. Components produced in WAAM are prone to different defects depending on the alloys used and overall have inferior mechanical properties when compared to parts produced through conventional processes [2]. One of those properties is hardness, which is a direct consequence of the resulting microstructure.

1.2 Objectives

This thesis aims to study the influence of shielding gas temperature in the microstructure and consequently on the hardness of parts produced during WAAM using metal inert gas (MIG) welding.

The major objectives are:

- To design and build systems capable of heating and cooling the shielding gas, and maintaining its temperature during depositions.

- To test the systems developed independently before using these during welding to assess their heating and cooling capacity.
- To study the effect of shielding gas temperature by producing and characterizing thin walls in terms of geometry, hardness and microstructure. This data is also to be correlated with the thermal cycles registered, using a thermographic camera to record depositions.

In order to assess this effect, both cooling and heating exchangers are to be tested with cooling/heating turned on and off. This will result in four conditions which are expected to be as shown in Figure 1.1. The undetermined values for X and Y are dependent on the cold and heat source, respectively.

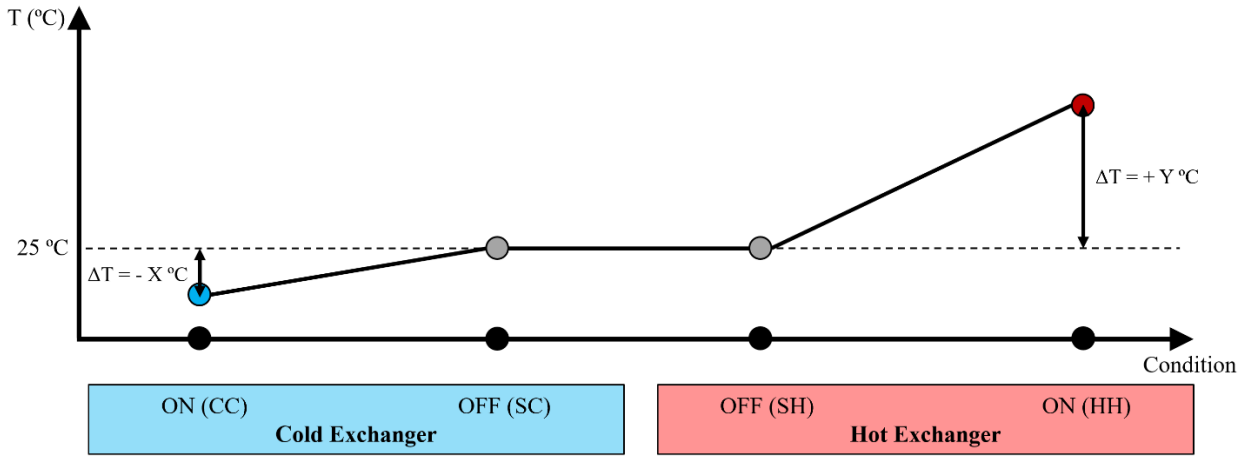

Figure 1.1: Working conditions available.

1.3 Document structure

This thesis is divided in five chapters.

Chapter 2 briefly describes the current status of wire and arc additive manufacturing. The most common issues are highlighted and solutions to these same issues presented.

Chapter 3 describes the equipment used and developed throughout this work as well as the characterization techniques used.

Chapter 4 presents and discusses the results obtained and finally conclusions and future work are presented in chapter 5.

2 Literature Review

In this chapter, a review of WAAM current status is presented and discussed. Common methods used to improve mechanical properties of components are then presented with emphasis on one of these methods, controlled cooling.

AM has been getting a growing interest both from the academic and industrial community due to the potential it unlocks. It allows the fabrication of complex metal components while saving material when compared to conventional existing processes.

2.1 Additive Manufacturing

Wire Arc Additive Manufacturing (WAAM) is an AM process that uses wire as feedstock and an electric arc as heat source. It distinguishes itself for its high deposition rates, low material and equipment costs, and a good structural integrity [1] making it a good alternative to current methods used to manufacture from solid billets or large forgings. Components produced using WAAM can also be lighter and therefore more efficient which could be critical when designing and building an airplane for example. A 2.5 m aluminum wing rib, which is usually produced through the machining of a solid billet, has a buy to fly (BTF) ratio of 37, needing 670 kg worth of material to produce the final part. By producing the same part using WAAM, a BTF ratio of 12 kg was achieved, which can be translated in saving of roughly 500 kg per part [1].

As referred previously, WAAM allows a high material deposition rate, usually higher than other AM processes, usually 1 kg/h for aluminum and 4 kg/h for steel. Hence, large components can be produced in reasonable times allowing time savings of 40-60% for fabrication processes and 15-20% for machining operations [2].

2.2 Current challenges of WAAM

Despite all the advantages, there are still some challenges associated with the production of components via WAAM. Without the proper measures and precautions, parts made using this process are prone to defects which can be detrimental to its function. This greatly reduces WAAM's scope of applications. The most common defects are porosities or the appearance of cracks or delaminations which can be caused by residual stresses, gas contamination or poor path planning. These defects have a greater or lesser preponderance depending on the materials used as shown on Figure 2.1.

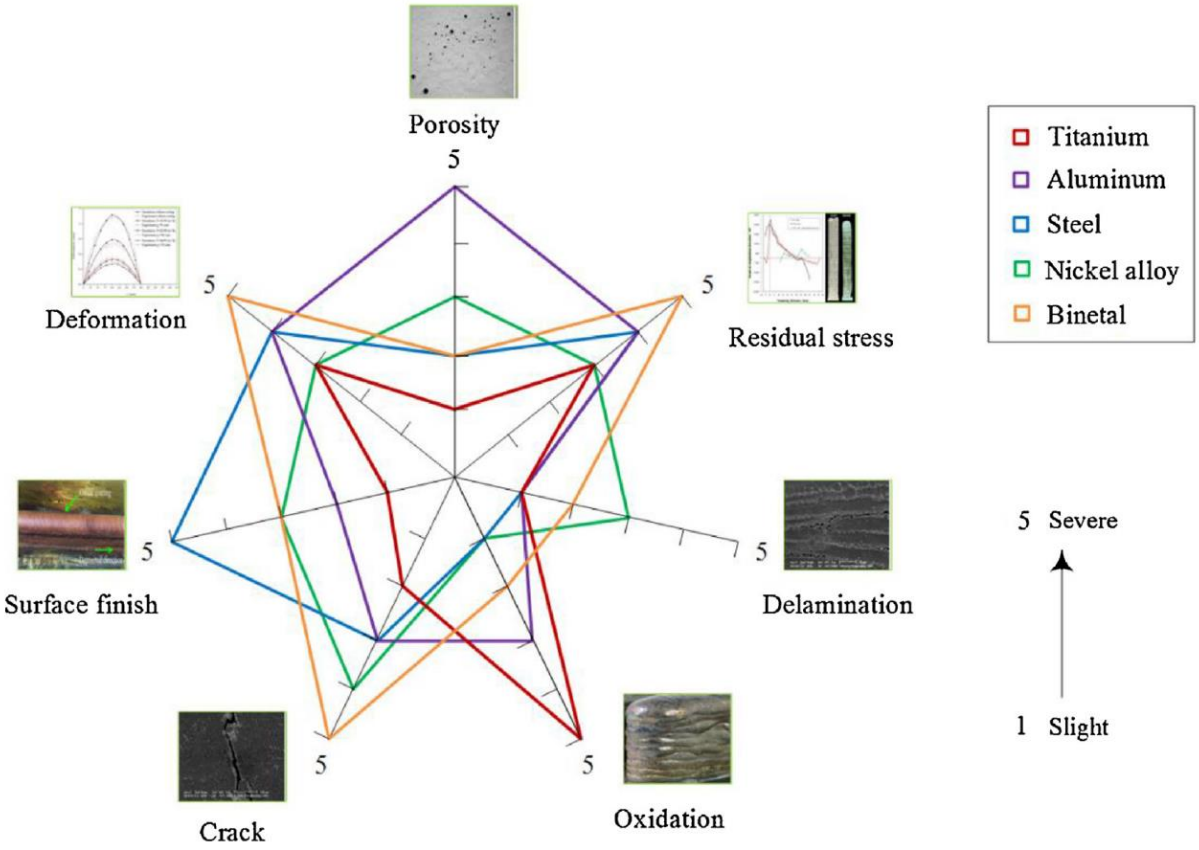

Figure 2.1: Correlation between materials and defects in WAAM processes [2].

The constant heating and cooling of the deposited material during the process causes expansion and contraction cycles that can create residual stresses on the part which will in turn influence the resulting mechanical properties and fatigue behaviour. If the residual stresses become greater than the local yield strength (YS), deformation or distortion will occur which may severely compromise geometrical tolerances of the part. In more extreme cases where residual stresses reach high values, cracks will occur making the component completely unusable [2].

The development of porosities within the part may cause a reduction on its strength as a result of existing micro-cracks and a decrease in the fatigue behaviour. The occurrence of these porosities may be due to the alloy chosen or the process itself. Impurities or humidity present in the wire's surface can find themselves mixed in the weld pool. When materials with lower solubility are used, as is the case with aluminum, when the temperature decreases the amount of dissolved particles in the weld pool may be greater than the solubility limit of the material, resulting in the formation of porosities [3].

Cracking or delamination between deposition layers are significantly influenced by the temperature distribution throughout the material during the process and by characteristics of the material itself. Cracking can therefore be sorted in two major groups, solidification and grain-boundary cracking. During solidification of the weld pool, the obstruction of the grain flow or occurrence of high stresses within the weld pool are the main causes for cracking. On the other hand, grain-boundary cracking develops mainly due to morphology differences within grain-boundary and possible incidences of precipitates or dissolutions in the weld pool. To minimize the prevalence of such cracks, the cooling rate can be controlled, or optimization processes can be made after producing the part. Regarding delamination, this is a type of defect that occurs when fusion of the pre-existent layer is incomplete. This type of defect can't be corrected after conclusion of the component, therefore measures must be taken during the process, such as pre-heating the subtract layer to guarantee its adequate fusion.

2.3 Common methods used to improve mechanical properties of components produced by WAAM

In order to improve mechanical properties and fix possible defects that occur during WAAM different processes can be used during or after manufacturing a component.

Nowadays, post-WAAM thermal treatment is the most common practice. This treatment increases the material's strength and allows the control of its hardness. In [4], the mechanical properties of an aluminum alloy from the 2000 series produced via WAAM were measured and subsequently compared to the ASTM norm for the same alloy produced by forging. Despite YS and UTS being initially inferior to the values within the ASTM norm, these values improved significantly after thermal treatment reaching values even higher than the ones defined by the ASTM standard. Results are as shown in Table 2.1.

Table 2.1: Mechanical properties of Al6.3Cu for different conditions (adapted from [2]).

Materials	Process	Condition	Microstructure	YS [MPa]	UTS [MPa]	EL [%]	Reported by
Al6.3Cu	Wrought (2219)	T851	/	267	390	> 4	ASTMB211M
	CMT	As fabricated	Fine dendrites + equiaxed grains	128 ± 2	262 ± 4	15.8 ± 0.3	Gu et al. [4]
				133 ± 5	264 ± 2	18.6 ± 1.5	
		Heat treated (T6)	Homogenous dispersed θ precipitates	305 ± 6	458 ± 3	13.6 ± 0.9	
				333 ± 6	466 ± 3	14	

Another process that can be used to improve mechanical properties is cold rolling. By using this process in between WAAM passes, also known as interpass rolling, microstructural refinement can be achieved [5]. This reduces residual stresses, distortions and allows for a greater isotropy in the resulting microstructure. The occurrence of porosities also decreases when cold rolling is used [6]. Geometry is the most limiting factor when considering the usage of this method, which can only be used for very simple and smooth components.

Forced interpass cooling can also offer significant improvements in the material's microstructure by allowing the control of thermal cycles. This method also reduces the occurrence of superficial oxidation and, in certain cases, increases productivity by reducing time between passes [5]. Figure 2.2 shows the effect of interpass cooling on hardness and UTS of a Ti6Al4V component produced with WAAM.

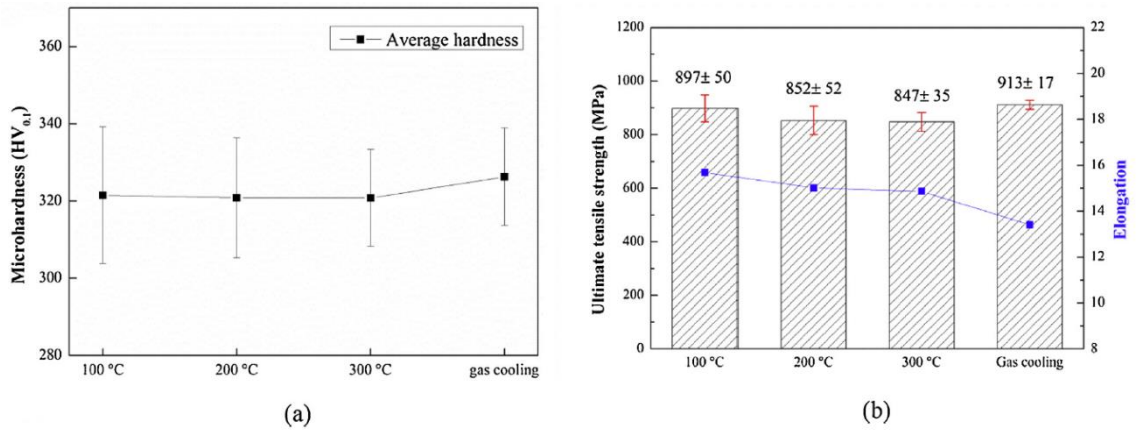

Figure 2.2: Mechanical Properties of a Ti6Al4V component produced with WAAM [7].

2.4 Controlled cooling

When a component is produced through WAAM, the deposited material is initially in a fused state, which means it will go through different state phases during its cooling. Such phases are dependent on variables such as pressure, thermal cycles, volume and chemical composition. In the context of WAAM, the two main variables that we can readily manipulate are thermal cycles and chemical composition.

2.4.1 Metastable iron-cementite diagram

Two types of iron-carbon equilibrium diagrams exist, the stable iron-graphite Fe-Gr and the metastable iron-cementite Fe-Fe_3C. The first diagram usually takes a very long time to develop which makes the later of more interest.

Steel is an alloy of iron with a certain carbon content depending on its grade. Although other elements are usually present in its composition, as is the case for 316L stainless steel which will be used in this study, the metastable iron-cementite phase diagram (Figure 2.3) can be very useful for understanding how temperature influences the resulting microstructure and consequently the component's mechanical properties. Phase is the term used to refer a portion of material with a distinct crystal structure which boundaries can be recognized. The most common phases for steel at room temperature are ferrite (α) and cementite (Fe_3C). Ferrite is a body-centered cubic (BCC) structure containing very little carbon which makes it almost pure in iron. This is the phase that confers ferromagnetism to steel. Cementite is an orthorhombic structure consisting of twelve iron atoms and four carbon atoms meaning it has an atom ratio of 3:1. This a hard and brittle phase that makes steel harder. The combination of ferrite and cementite is called perlite, which is composed of alternating layers of the two phases, therefore perlite is not a phase. Steel with exactly 0.77 wt.% carbon content will result in uniform perlite at room temperature.

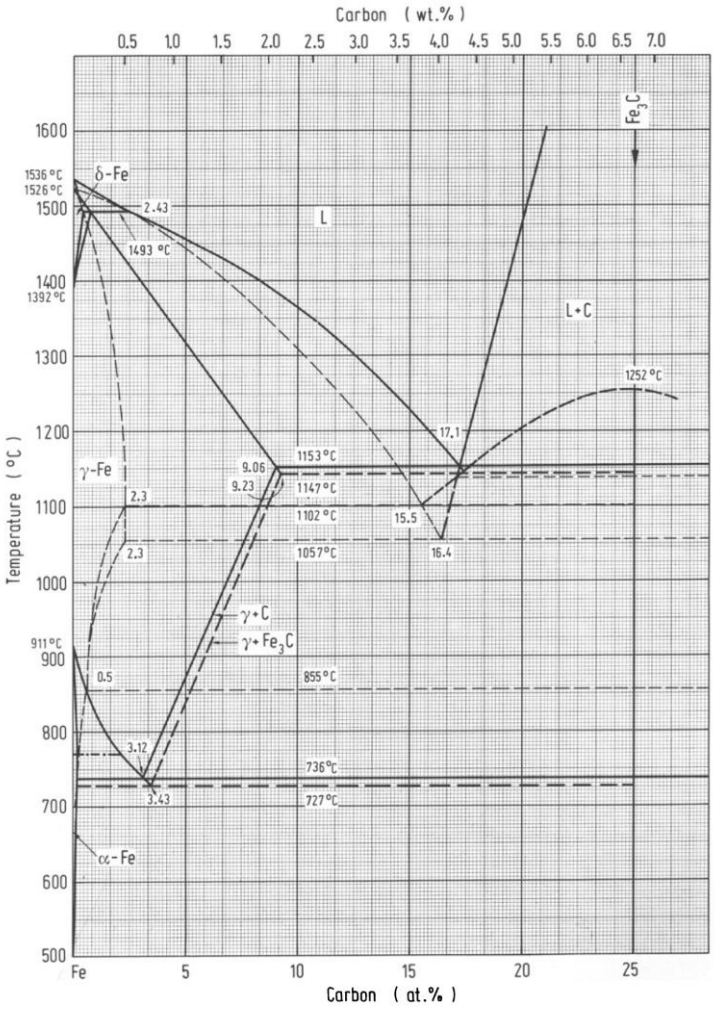

Figure 2.3: Metastable iron-cementite diagram [8].

Ferrite and cementite phases are the result of a slow and controlled cooling of the steel from a temperature higher than the austenitization temperature. Austenitization is also the name given to the process of heating steel to a temperature where the crystal structure changes from a combination of ferrite and cementite to austenite. Austenite is only possible to form at high temperatures and displays a face-centered cubic (FCC) structure. If instead of a slow cooling, the austenitic steel is quickly quenched, carbon atoms don't have enough time to diffuse out of the crystal structure in large enough quantities to form cementite and the resulting structure is martensite [9]. This phase is known for its very high hardness and brittleness which is due to its needle-like microstructure. In order to recover some toughness, tempering is required, during which steel is reheated to sub-austenitic temperatures. To obtain steel with very similar properties to tempered martensite, instead of quenching the material directly from austenitic temperatures to room temperature, quenching can be made to intermediate temperatures and held for a certain period of time. If carbon steel AISI 1050 for example is quenched from 800ºC to 400ºC and held

at that temperature for over 100 s, bainite is formed as shown in Figure 2.4. Bainite is a microstructure that has shown to have very similar properties as tempered martensite, although the latter has the potential to be harder and therefore stronger.

Mechanical properties of a given material are a direct consequence of its microstructure. Being the microstructure highly dependent on thermal cycles suffered throughout the different stages of production, it is important to understand the full effect of every small variation on the thermal cycles.

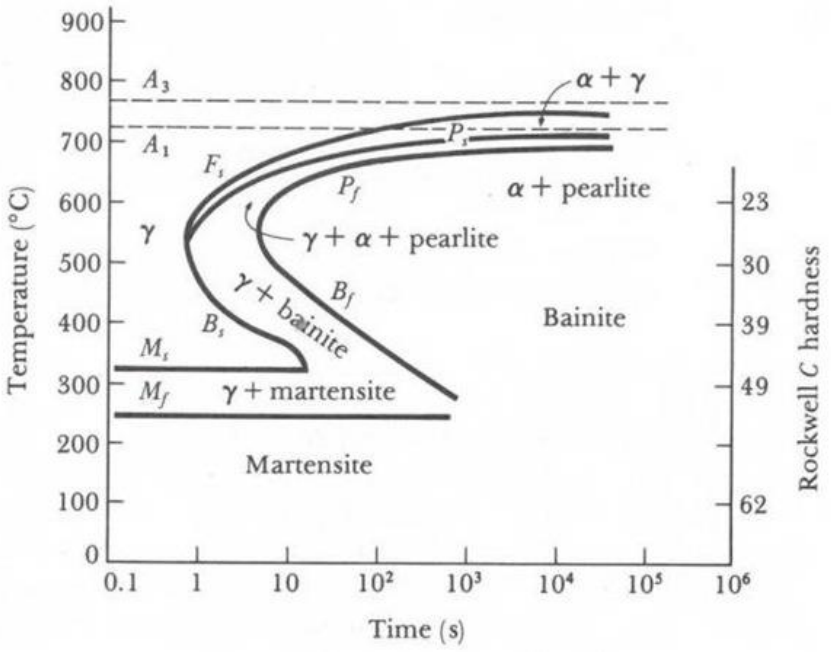

Figure 2.4: TTT diagram for AISI 1050 steel [10].

2.4.2 Cooling rate effect on the mechanical properties of metal

Several studies have been made to understand the effect of cooling rate on metals. Back in 1987, Umemoto et al. studied the effect of cooling rate on grain size of ferrite in a carbon steel [11]. A commercial 0.15% C steel (S15C) was used with the chemical composition shown in Table 2.2 from which sample rods with Φ3 mm x 10 mm were machined. Samples were austenitized at different temperatures (1423, 1373 or 1323 K) for 15 min and cooled at different rates (from 0.05 to 30 K/s).

Table 2.2: Chemical composition of S15C steel [11].

C	Si	Mn	P	S	Cr	Ni	Al	Cu
0·15	<0·1	0·40	0·009	0·011	0·02	0·02	...	0·01

By only varying austenitization temperature, a decrease in austenite grain size with a decrease in austenitization temperature was observed through optical micrographs (Figure 2.5 (a)). A subsequent decrease in ferrite grain size was also observed demonstrating a relation between austenitization temperature and ferrite grain size as illustrated in Figure 2.5 (b).

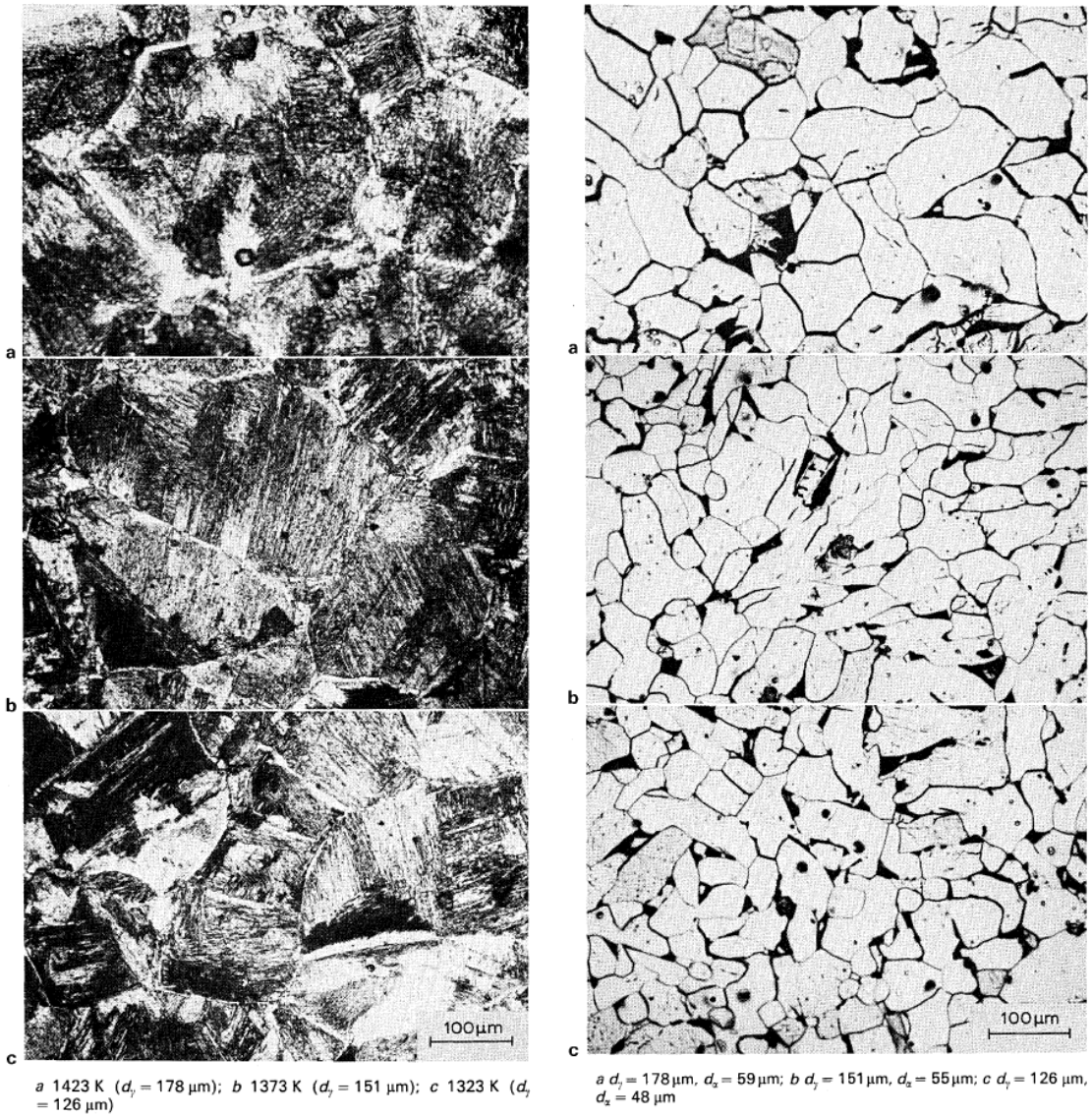

(a) (b)

Figure 2.5: (a) Austenite grains formed for different austenitization temperatures [11], (b) Ferrite grains formed for different austenitization temperatures [11]

By varying the cooling rate, an inverse proportionality between cooling speed and grain size was observed as shown in Figure 2.6.

Through mathematical analysis, Umemoto et al. were able to calculate the relation between ferrite grain size and both austenitization temperature and cooling rate, resulting in equation (2.1) where d_α is the ferrite grain size, d_γ the austenite grain size and q the cooling rate.

$$d_\alpha = 5.7q^{-0.26}{d_\gamma}^{0.46} \quad (2.1)$$

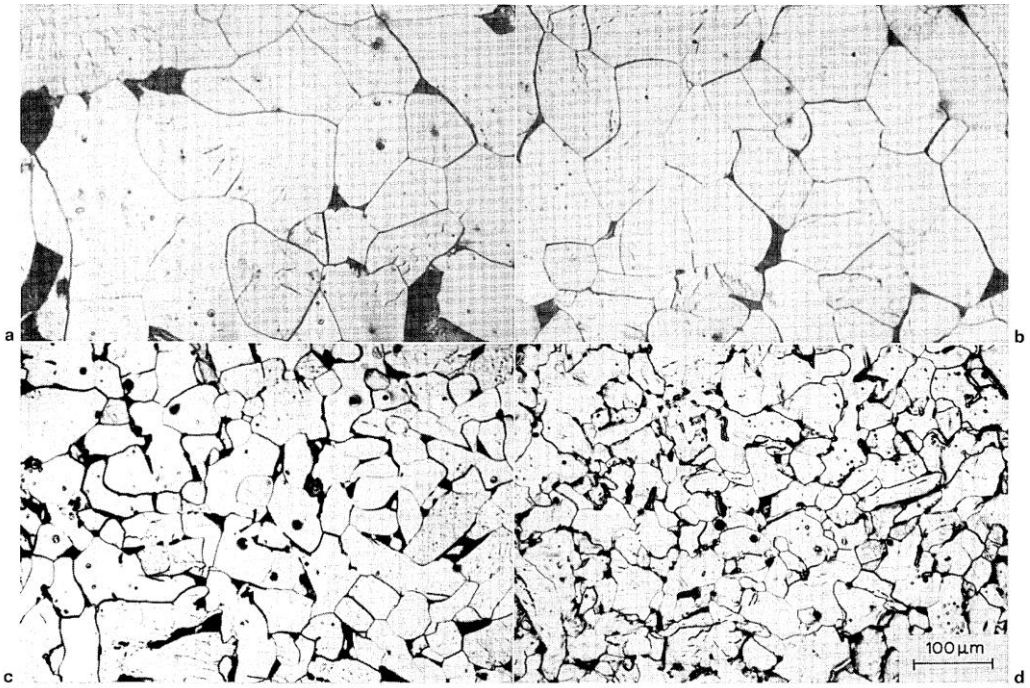

a 0·05 K s^{-1} (d_α = 106 µm); *b* 0·17 K s^{-1} (d_α = 79 µm); *c* 1·25 K s^{-1} (d_α = 48 µm); *d* 5·0 K s^{-1} (d_α = 33 µm)

Figure 2.6: Ferrite grains formed by cooling at different rates for samples austenitized at 1323 K [11].

More recently, Di et al. (2015) demonstrated the influence of cooling rate on microstructure, inclusions and mechanical properties of weld metal in simulated local dry underwater welding [12]. To control the cooling rate, both heat input and cooling environment were manipulated. Three different heat inputs were used, 10, 20 and 30 kJ/cm and two cooling environments were imposed, air and water cooling. This resulted in a total of 6 samples as shown in Table 2.3.

Table 2.3: Welding parameters and heat input [12].

Sample	Welding current *I*/A	Welding voltage *U*/V	Welding speed *v*/(cm/min)	Heat input E/(kJ/cm)	Cooling rate $t_{8/5}$/s
AC10	215	24.9	27.0	10.0	10.0
AC20	215	24.9	13.2	20.0	15.7
AC30	275	28.9	13.2	30.0	24.6
WC10	215	24.9	27.0	10.0	8.6
WC20	215	24.9	13.2	20.0	10.3
WC30	275	28.9	13.2	30.0	14.5

Regarding mechanical properties, Vickers method (HV10) was used to measure hardness and a Charpy impact testing was used to measure toughness. Both measurements showed an increase in both hardness and toughness for samples with higher cooling rates as shown in Table 2.4 and Figure 2.7. This was associated with an increase in acicular ferrite and decrease in proeutectoid ferrite and ferrite side plate.

Table 2.4: Hardness results for different samples [12].

Samples	AC10	AC20	AC30	WC10	WC20	WC30
Hardness	198 ± 12	188 ± 9	187 ± 10	221 ± 23	203 ± 9	200 ± 5

Ertyuiop+

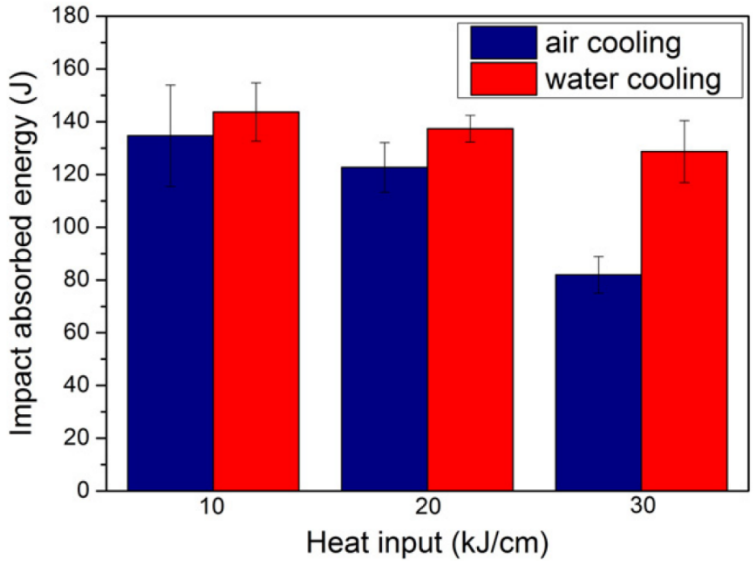

Figure 2.7: Impact absorbed energy -20 ºC [12].

2.5 Chapter summary and conclusion remarks

With high deposition rates, lower production costs when compared to conventional processes and good structural integrity, WAAM processes are increasingly being used. But despite all of its advantages, there are still challenges that need to be addressed.

It has been shown that cooling rate can not only influence the type of microstructure, but also the resulting grain size, independently on the predominant phases present in the microstructure. It is generally a variable easy to control which makes it very relevant to study its influence on every process that involves metal fusion.

Within the context of WAAM, designing a functional adjustable cooling system will be very beneficial to the continuing development and improvement of WAAM processes. This work aims to contribute to such system development.

3 Experimental procedure

This chapter describes the welding equipment and consumable materials used throughout this work. Characterization techniques and calculations used to develop the heat exchangers used and to determine heat input and deposition rate are also detailed, as well as the deposition strategy.

3.1 Welding equipment

The welding machine used was from *KEMPY, Pro MIG 501* (wire feeder and control unit) and *Pro MIG 3200* (power source). This equipment can work with three different MIG welding options, synergic continuous wave, synergic pulsed wave and conventional continuous wave mode. In the conventional mode, both the wire feed speed (WFS) and the voltage can be set independently. In synergic mode only the WFS can be freely selected while the voltage and current can only be slightly adjusted.

A customizable torch, which was developed in the context of Valdemar Duarte PhD thesis, consisting of a knob gear that clamps and extrudes wire through the nozzle was used, allowing the use of different materials and enabling minor tweaks to be made such as using different nozzles and/or attaching additional components.

To guarantee repeatability a three-axis machine controlled by *Repetier Host* software was used to control the torch travel speed and wire feed speed using G-code.

3.2 Materials

Every deposition was made using a structural steel plate with the dimensions 220×100×8 mm used as a substrate. Two types of consumable solid wire, 316L stainless steel and Inconel 625 superalloy were used to assess the effect shielding gas temperature. Their composition is shown in Table 3.1 and Table 3.2 respectively. The shielding gas used was commercial pure Argon with a chemical composition as shown on Table 3.3 and a gas flow rate (GFR) of 20 L min^{-1}.

Table 3.1: Chemical composition of 316L stainless steel.

Chemical composition (wt. %)								
C	Mn	Si	P	S	Cr	Mo	Ni	N
0.03	1.80	0.75	0.045	0.03	18.50	2.6	12.5	0.1

Table 3.2: Chemical composition of Inconel 625.

Chemical composition (wt. %)											
Ni	Cr	Mo	Co	Nb	Al	Ti	C	Fe	Mn	Si	Cu
>58	21.5	9	1	3.5	0.4	0.4	0.1	5	0.5	0.5	0.5

Table 3.3: Shielding gas composition.

Alphagaz 1	Ar	H_2O	O_2	C_nH_m
	99.999 %	<3 ppm	<2 ppm	<0.5 ppm

3.3 Characterization techniques

3.3.1 Microstructure characterization

Each sample was prepared by being cut, grinded and polished using up to P2500 sandpaper after which diamond polishing paste was used. Inconel 625 samples were then etched using a mixture of 15 mL HCl, 10 mL acetic acid and 10 mL HNO_3 while 316L samples were etched using Vilella's reagent (1 g Picric acid, 5 mL HCl in 100 mL ethanol). Optical microscope Leica DMI5000 M was then used to analyze the microstructure of the walls produced.

3.3.2 Microhardness measurements

To measure microhardness, a *Mitutoyo HM-112 Micro-Vickers Hardness Testing Machine* was used. Indentations were made from the base of each wall up to its top within the dashed line's region shown in Figure 3.1, with intervals of 500 μm between indentations and using a load of 0.5 Kg applied during 10 s for every measurement.

Figure 3.1: Indentations guide line.

3.3.3 Thermography

Being able to monitor the temperature during depositions is essential in order to determine the effect of the shielding gas temperature on thermal cycles suffered by the produced components. A *Fluke TI400* infrared camera was therefore used to measure the temperature of both the beads and the surrounding elements (such as the torch nozzle) during each deposition. The emissivity was set to 0.84 [13], and the range to a maximum of 1200ºC with a measurement accuracy of ± 2ºC. The camera was placed 1 m away from the welding area and videos of the entire depositions were recorded. Data was later collected from the videos through *SmartView* software which allowed to select specific points in each layer and collect every temperature with a 9 Hz frequency. This data was then used to make graphs using *Microsoft Excel (2016)*.

3.4 Heating and cooling of shielding gases

To control the cooling rate of parts produced through WAAM, an initial system injecting cold/hot air directly on each layer was attempted, but due to the high influence of the air flow on the shielding gases flow, the produced parts displayed high porosity which meant the system was unviable. In order to avoid this phenomenon, a system capable of cooling and heating the shielding gases themselves was designed and tested using two different materials.

Steel melts at temperatures over 1500 ºC, therefore thermal inertia is more favorable when attempting to heat a gas during this process. This is not true for the opposite case where we try to

cool a gas and maintain its temperature, therefore two different solutions were implemented despite both consisting of heat exchangers.

3.4.1 Heat exchange calculations

Simple approximations were used to design and build the two heat exchangers used throughout this work. The rate of heat transfer, q, can be written as:

$$q = UA(T_s - T_{f,\infty}) \qquad [\mathrm{W}] \qquad (3.1)$$

Where U [W m^{-2} K^{-1}] is the overall heat transfer coefficient, A [m^2] is the surface area in contact with fluid, T_s [K] is the surface temperature, $T_{f,\infty}$ [K] is the temperature of undisturbed fluid far away from the heat transfer surface. To increase the surface area a helical-coil heat exchanger was chosen to heat/cool welding gases. Therefore, A was given by the following equation:

$$A = \pi\, d\, L \qquad [\mathrm{m}^2] \qquad (3.2)$$

Where d [m] is the tube diameter, L [m] is the tube length.

To determine the necessary rate of heat transfer, simple calorimetry was used:

$$q = \dot{m}\, c_p\, \Delta T \qquad [\mathrm{W}] \qquad (3.3)$$

Where $\dot{m}$ is the mass flow rate of the shielding gas [Kg m^{-3} s^{-1}], c_p is the shielding gas heat capacity [J Kg^{-1} K^{-1}], ΔT is the temperature rise or drop [K].

Every variable was known except for the overall heat transfer coefficient U and the tube length L. For the chosen application, U would have a value between 150-500 according to Table 3.4, but a much lower value of 15 W m^{-2} K^{-1} was chosen to make sure that the final heat transfer rate was enough to cool or heat the shielding gas to the desired temperature.

Table 3.4: Overall heat transfer coefficient for tubular heat transfer types (adapted from [14]).

Application	**Overall Heat Transfer Coefficient [W m^{-2} K^{-1}]**
Gas at atmospheric pressure inside and outside tubes	5 – 35
Gas at high pressure inside and outside tubes	150 – 500
Liquid outside/inside and gas at atmospheric pressure inside/outside tubes	15 – 70
Gas at high pressure inside and liquid outside tubes	200 – 400
Liquids inside and outside tubes	150 – 1200
Steam outside and liquid inside tubes	300 – 1200

L was calculated by equating equations (3.1) and (3.3), resulting in equation (3.4):

$$UA\left(T_s - T_{f,\infty}\right) = \dot{m}\, c_p\, \Delta T \rightarrow\ A = \frac{\dot{m}\, c_p}{U} \tag{3.4}$$

Note: $\Delta T \sim \left(T_s - T_{f,\infty}\right)$

Replacing A with equation (3.2), L is given by:

$$L = \frac{\dot{m}\, c_p}{U\, \pi\, d} \qquad [\text{m}] \tag{3.5}$$

3.4.2 Heat exchangers building

The tube used to make both heat exchangers was made from copper and had an outside diameter of 8 mm. The shielding gas had an average GFR of 20 L min^{-1}, which, replacing by argon's density of 1.7835 Kg m^{-3} corresponded to a mass flow of 5.95×10^{4} Kg s^{-1}. Argon's specific heat capacity is approximately 520 J Kg^{-1} K^{-1}.

The minimum necessary tube length was therefore estimated by replacing equation (3.5) with the respective values mentioned above:

$$L = \frac{5.95 \times 10^{-4} \times 520}{15 \times\ \pi \times 0.008} \cong 0.82 \quad [\text{m}] \tag{3.6}$$

Hot exchanger – Heat exchanger to heat argon

A metalworking lathe was used to roll the copper tube into a helical coil with a diameter of approximately 55 mm, which was then placed inside a Φ120×200 mm aluminum tube with a wall thickness of 5 mm covered on the inside with 2 layers of *Superwool blanket* to minimize heat exchanges with the surrounding atmosphere. The two covers were held together by a steel threaded rod M6×220 mm with screwed hex nuts on both sides as shown in

Figure 3.2. To avoid interference with the shielding gas flux, the outlet hole was covered with a flexible aluminum tubing allowing it to be redirected away from the weld pool. *Ufesa ESSENTIAL ION 2200W SC8348/01* hairdryer was used to generate a hot gas. To avoid malfunction from excessive heat accumulation, the original plastic cover was replaced by a thin steel sheet as shown in Figure 3.3 and the safety protection circuit was shorted to enable the hairdryer to work indefinitely. The final result is shown Figure 3.4 ready to be used.

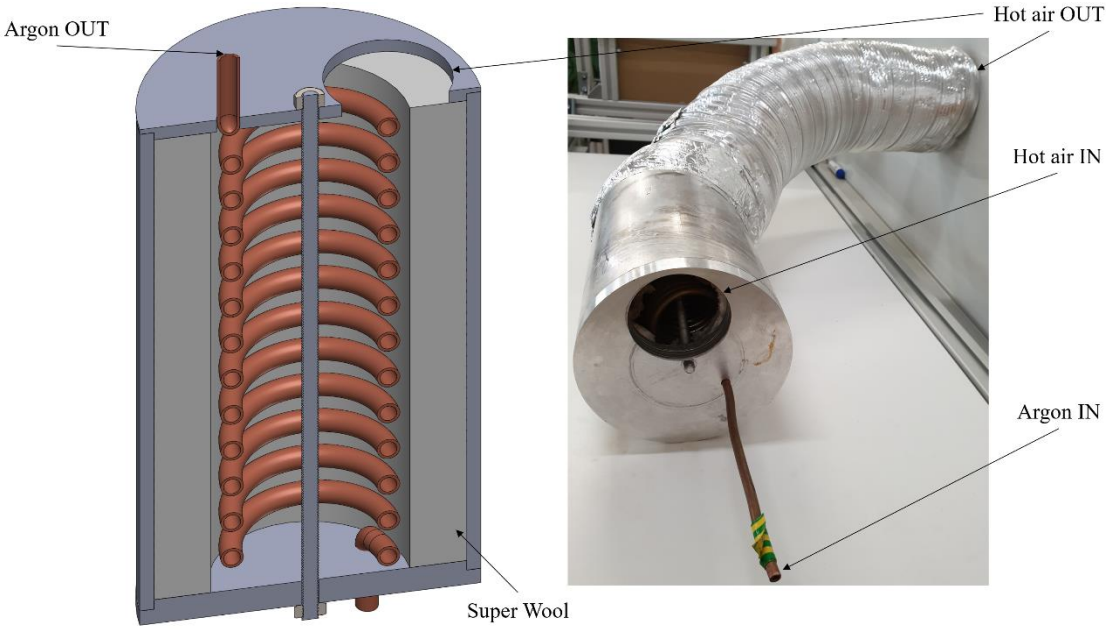

Figure 3.2: SolidWorks sectional view and final result of heat exchanger used to heat argon.

Figure 3.3: Modified hairdryer.

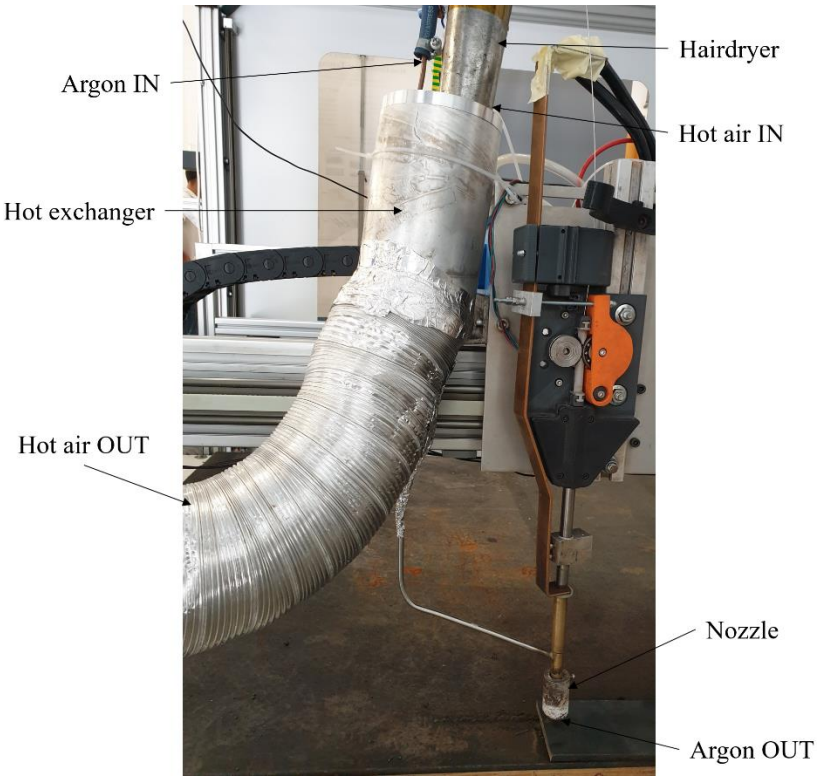

Figure 3.4: Heat exchanger ready to heat argon.

Cold exchanger – Heat exchanger to cool argon

As mentioned above, thermal inertia is not favorable when trying to cool and hold argon at a low temperature given the high temperatures reached when arc welding. Such temperatures cause involved components, such as the nozzle to heat up to temperatures higher than 200ºC. Given that the shielding gas comes in contact with such components and given how low argon's specific heat is (520 J Kg^{-1} K^{-1}), a new approach was attempted.

Cold air was produced by the action of a *Meech* pneumatic cold fraction vortex tube (Figure 3.5) capable of reaching temperatures as low as -16ºC when tested at DEMI-FCT NOVA.

To maintain the cold inertia produced by the vortex tube, the nozzle itself was converted into a heat exchanger by involving the inside cup with helical coils such as the ones used for heat exchanger 1, and isolating them with a second steel cup covered with super wool to reduce heat exchanges with the outside. To hold the super wool, an aluminum tape was used.

This heat exchanger was designed to work in counter flow mode to maximize its cooling capacity. Cold air enters through the top and exits through a hole on the bottom and is then redirected upwards by a welded tube piece that also guides the copper coil entrance as shown in

Figure 3.66. The final result is shown in Figure 3.7.

Figure 3.5: *Meech* pneumatic cold fraction vortex tube.

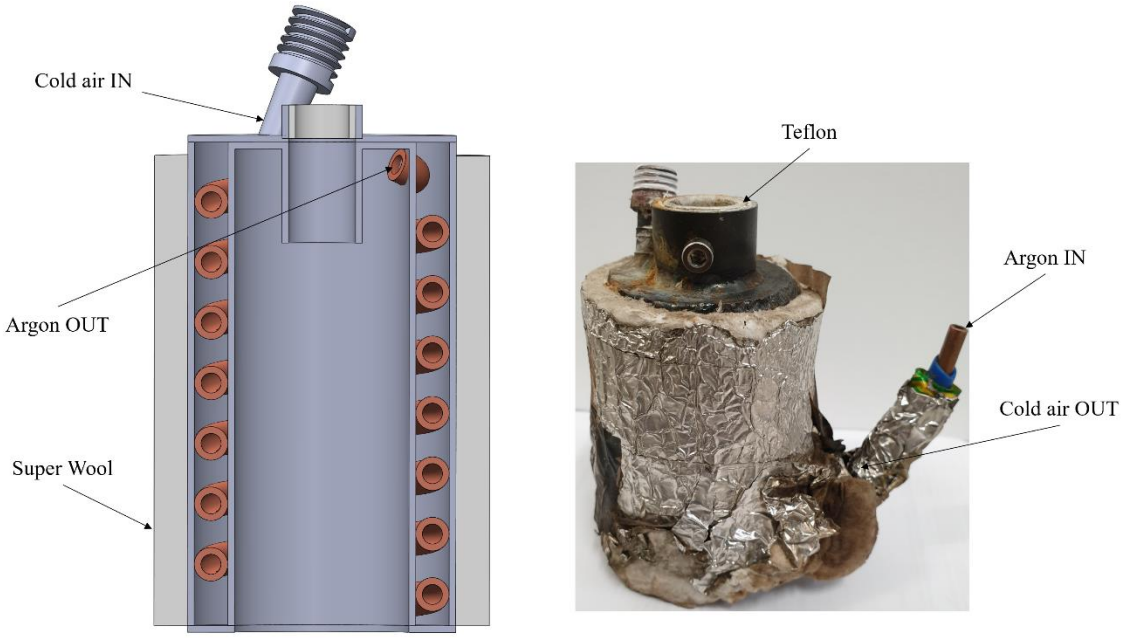

Figure 3.6: SolidWorks sectional view and final result of heat exchanger used to cool argon.

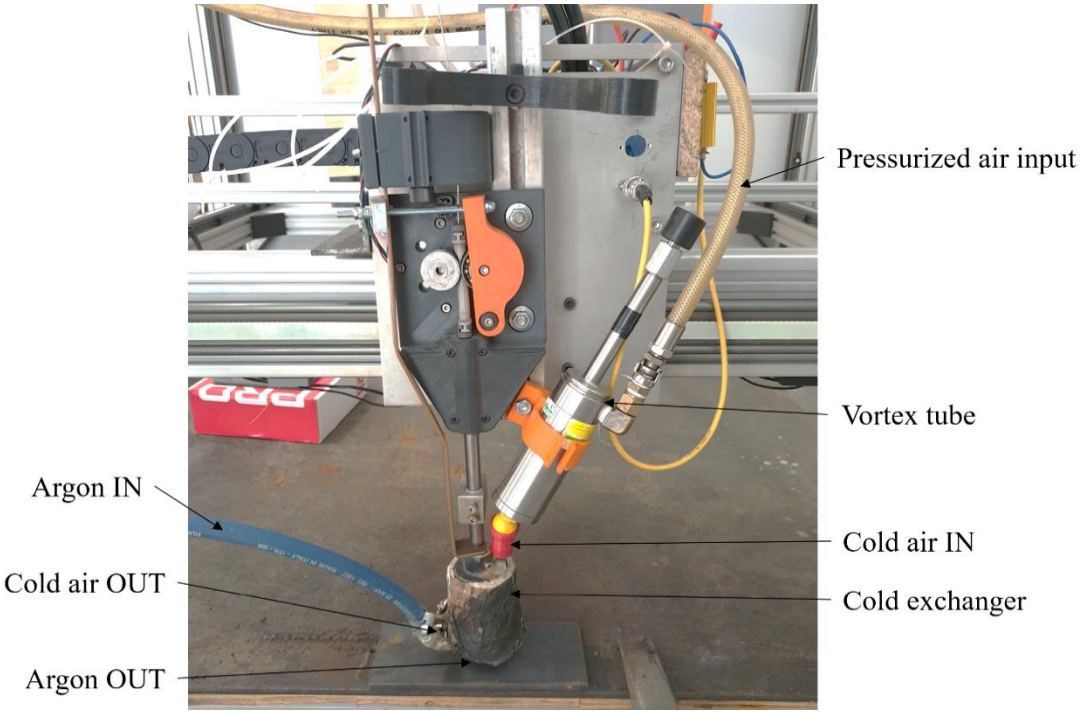

Figure 3.7: Cooling system ready to be used.

3.5 Deposition strategy

Metal deposition was made in both directions to guarantee uniform height throughout the length of the wall produced, as shown in Figure 3.8, and the interpass cooling time was set to 1 minute. The contact tip to work distance was set at approximately 10 mm and the wall length was fixed at 150 mm.

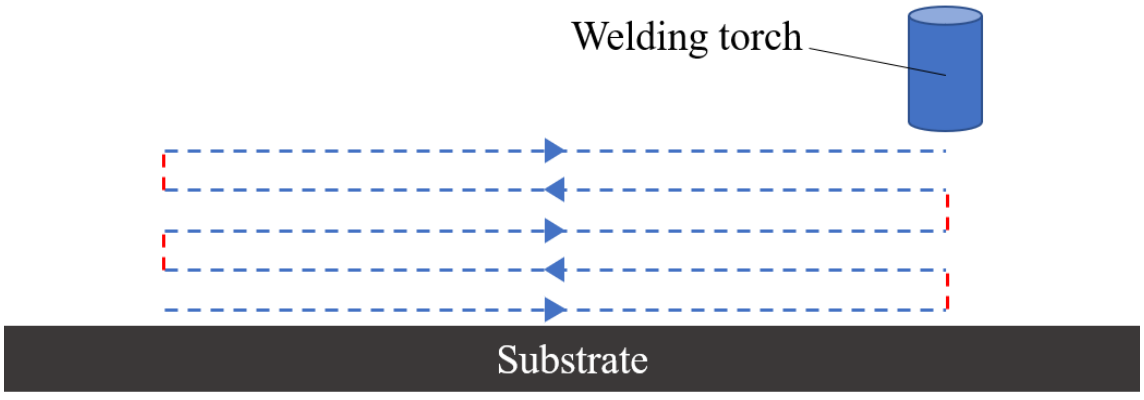

Figure 3.8: Deposition path.

3.6 Heat input and deposition rate

Heat input was calculated using equation (3.7).

$$HI = \frac{U \times I}{TS} \times \eta \qquad [J\ mm^{-1}] \qquad (3.7)$$

Where U is the RMS of the voltage [V], I the RMS of the current [A], η the welding process efficiency and TS the travel speed [$mm\ s^{-1}$].

The deposition rate, DR, was calculated by dividing the mass of a layer by the time each deposition takes resulting in equation (3.8).

$$DR = \frac{WFS \times \pi \times D^2 \times \rho \times 60}{4} \qquad [Kg\ h^{-1}] \qquad (3.8)$$

Where WFS is the wire feed speed [$m\ min^{-1}$], D is the wire diameter [m] and ρ the consumable wire density [$Kg\ m^{-3}$].

4 Results and discussion

In this chapter, heat exchanger testing results are presented and discussed. Process parameters for every deposition are also presented and results for each material are shown and discussed. A power comparison between the heating/cooling power of the heat exchangers used and power involved during arc welding is made to give context and a better notion of how significant involved temperature variations are.

4.1 Heat exchanger testing

Both heat exchangers were tested before being used in welding to determine their heating or cooling capacity. This was done by using thermocouples attached both to the standard and the cooling nozzle's exit as shown in Figure 4.1.

Figure 4.1: Thermocouple measuring temperature of hot argon at nozzle's exit.

Using heat exchanger 1, argon was successfully heated to a maximum temperature of 92.66 ºC taking just a little over 1 minute to reach 90 ºC as shown in Figure 4.2. This represented an increase of 67 ºC

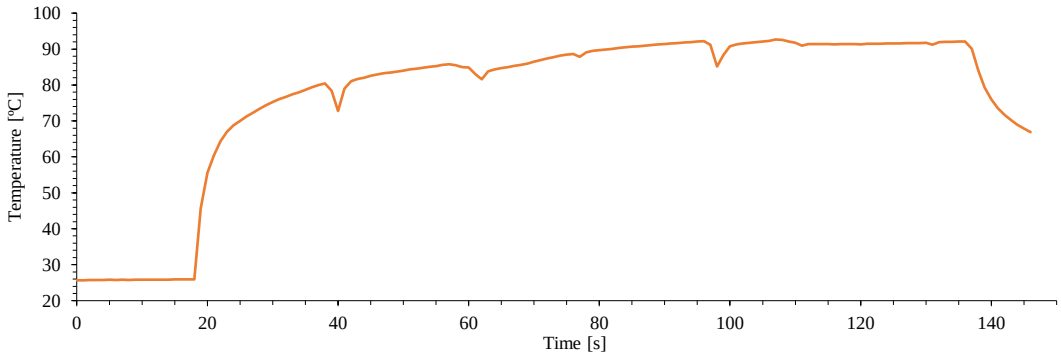

Figure 4.2: Argon temperature at nozzle exit using heat exchanger 1.

Data on Figure 4.3 shows several peaks for the first 2 minutes because the vortex tube generating cold air was calibrated throughout this measurement, and the correct position for the hot end valve, which regulates the ratio between cold and hot air, was only obtained at approximately 122 s. Plotted points situated before this time are not relevant which is why some points are out of range.

The cooling system was much slower than heating, taking 409 s for argon to reach the minimum temperature recorded which corresponded to -2.28 ºC and -8.6 ºC for the nozzle (heat exchanger). It is worth nothing that temperatures were still going down but at a very slow and decreasing rate.

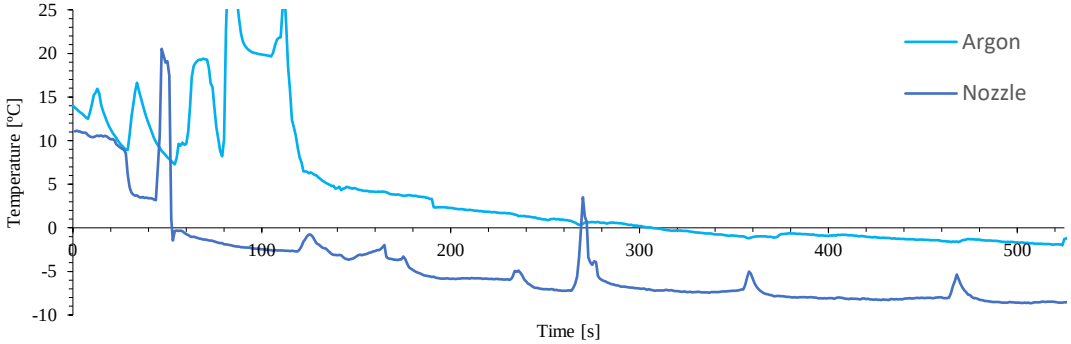

Figure 4.3: Argon temperature evolution using heat exchanger 2.

Gas flow at the nozzle exit was also studied given that the cooling exchanger was unable to be connected to a diffuser, instead, gas was injected at an angle of the upper region within the nozzle. This increased turbulence on the gas flow which was observed using chalk powder and

pressurized air to simulate the path taken by shielding gas. The gas streamlines should look like shown in Figure 4.3. Through the usage of a diffuser, the gas flow is laminar, which isn't the case for the cooling nozzle given the entry angle which causes the flow to follow a helical path increasing turbulence.

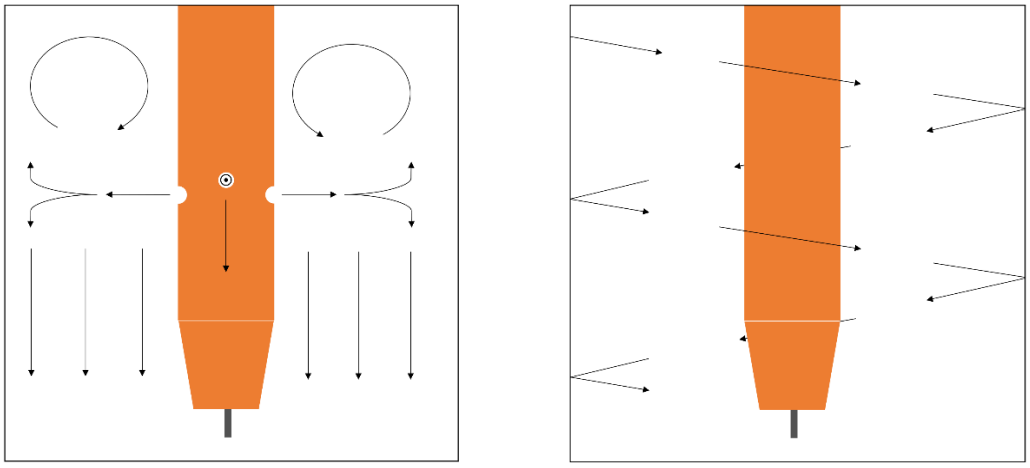

(a) (b)

Figure 4.4: Streamlines comparison within (a) regular nozzle, (b) cooling nozzle.

4.2 Process parameters and sample references

All the depositions were made with the same process parameters (shown in Table 4.1), except for the shielding gas temperature which depended on the heat exchanger used and, on its status (on/off). A total of 8 samples were obtained, 4 for each alloy as shown in Table 4.2. A standard sample where gas was neither cooled or heated was made for both systems to assess if results were not due to a potential pressure loss or due to the gas flow itself which was different for the cooling system.

The choice of letters to designate different samples is also explained in Table 4.3 to help understand the nomenclature.

Table 4.1: Process parameters used.

Process parameters					
Gas	GFR [L/min]	WFS [m/min]	TS [mm/s]	Voltage [V]	Heat input [J/mm]
Alphagaz 1	20	4	5	19	640

Table 4.2: Sample references.

Sample	Alloy	Heat exchanger	Heating/cooling status
HH-S	316L SS	1	ON
SH-S	316L SS	1	OFF
SC-S	316L SS	2	OFF
CC-S	316L SS	2	ON
HH-I	Inconel 625	1	ON
SH-I	Inconel 625	1	OFF
SC-I	Inconel 625	2	OFF
CC-I	Inconel 625	2	ON

Table 4.3: Sample references explanation.

Nomenclature	Meaning
HH	**H**ot gas **H**ot exchanger
SH	**S**tandard gas **H**ot exchanger
CC	**C**old gas **C**old exchanger
SC	**S**tandard gas **C**old exchanger
xx-**I**	**I**nconel 625 sample
xx-**S**	316L stainless **S**teel sample

4.3 Depositions with 316L stainless steel

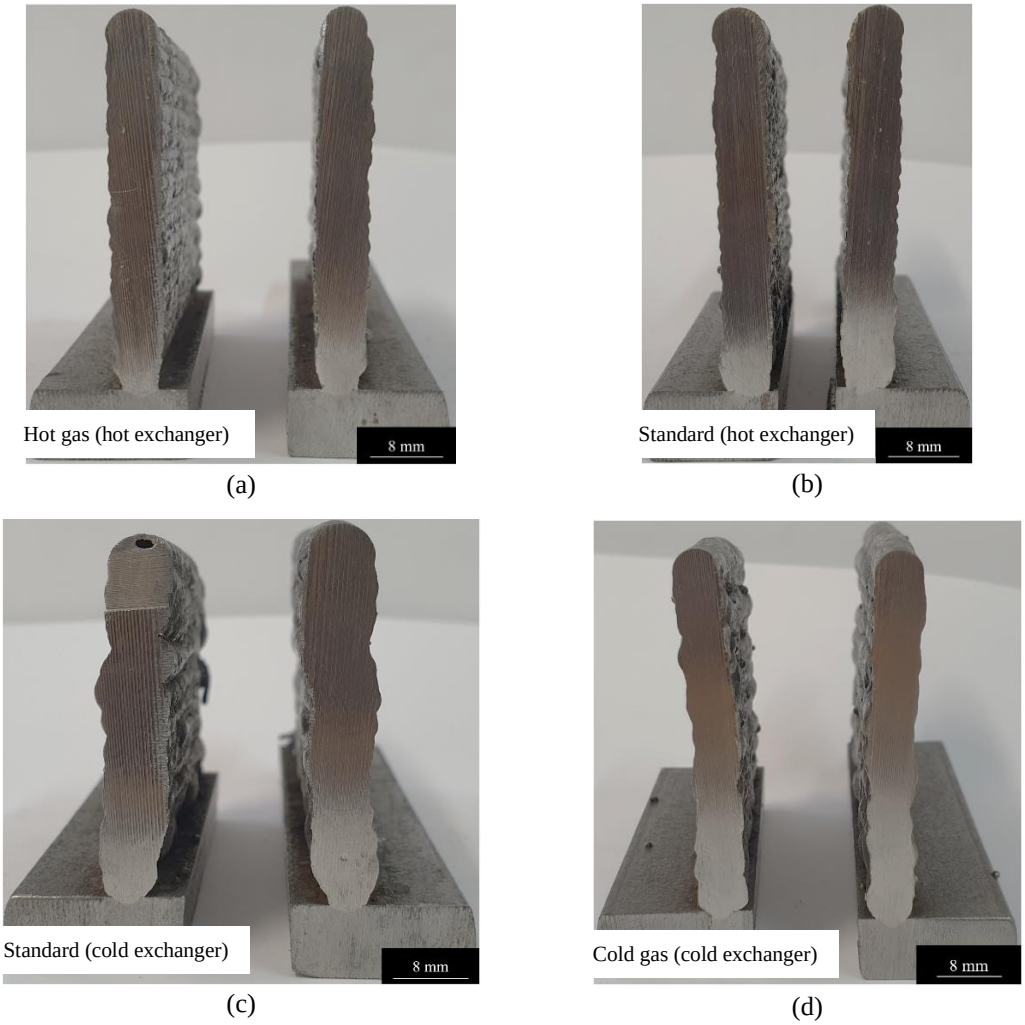

Figure 4.5: Transversal section of sample HH-S (a), SH-S (b), SC-S (c) and CC-S (d).

Results for depositions made with 316L stainless steel are shown in Figure 4.5. A very clear difference was visible by eye between samples CC-S and SC-S, the first being significantly taller and thinner while also displaying less waviness. No noticeable difference was detected at the naked eye between SH-S and HH-S, but a decrease in waviness was noticeable for these samples when compared to the two samples produced using heat exchanger 2.

The height of each sample was manually measured using a ruler, while the effective wall width (EWW) was measured according to Wu et al. [15] schematic using *Adobe Photoshop CC 2019* as shown in Figure 4.6. As shown in Table 4.4, the sample produced using cold argon (CC-S) was approximately 15.8 % taller and 14.4 % thinner than the sample in which the gas was injected at standard room temperature (SC-S). The differences between the samples produced using the heating system weren't significant (both smaller than 5 %).

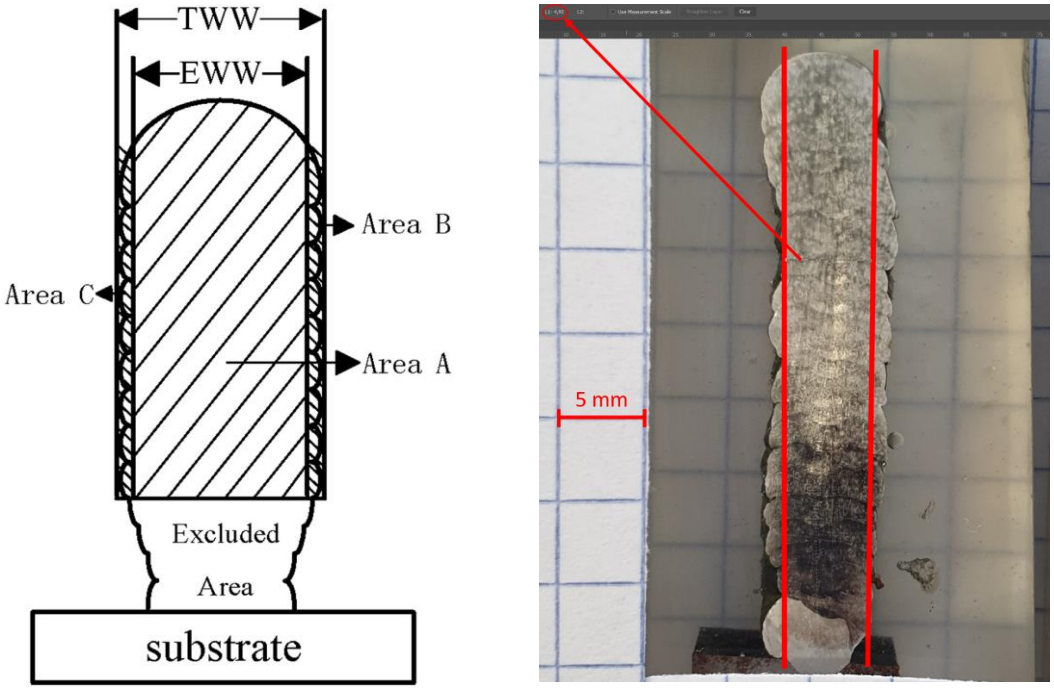

(a) (b)

Figure 4.6: EWW (a) EWW schematic [15], (b) measurement example.

Table 4.4: Average height and EWW of 316L samples.

Sample	EWW [mm]	Height [mm]
HH-S	4.62	42
SH-S	4.84	44
SC-S	5.2	38
CC-S	4.45	44

It is worth nothing that although a difference was expected between CC-S and SC-S, SC-S and SH-S were expected to be very similar samples given that in both cases argon was injected at room temperature.

4.3.1 Thermography results

Thermography results were used to draw temperature and cooling rate graphics. Figure 4.7 displays the temperature evolution tracking points located in layer 5 (a) and layer 15 (b) for samples produced with the cooling exchanger. The first peak corresponds to the layer deposition, and the following peaks to every successive deposition. In Figure 4.7 (a), curves are slightly out

of phase which is a result of a minor technical complication which happened after the deposition of layer 8 for sample SC-S, and doubled the interpass cooling time for that particular layer.

A very significant difference was observed between the 2 curves for both layer 5 and 15 tracking points. With cooling turned on, the upper peak values of sample CC-S for subsequent passes were significantly lower than values registered for SC-S. Even with the increased overpass time that occurred at minute 8 during SC-S depositions due to a minor technical complication, the following peak reached a higher temperature than the corresponding CC-S peak. As a consequence, CC-S layers resided for a lesser amount of time within the 800-500 ºC interval which should result in differences within the microstructure and consequently on microhardness results.

The same data was collected for samples SH-S and HH-S, produced with the hot exchanger, and is presented in Figure 4.8. No significant difference was observed besides a very slight increase in temperature for the upper peaks corresponding to sample HH-S.

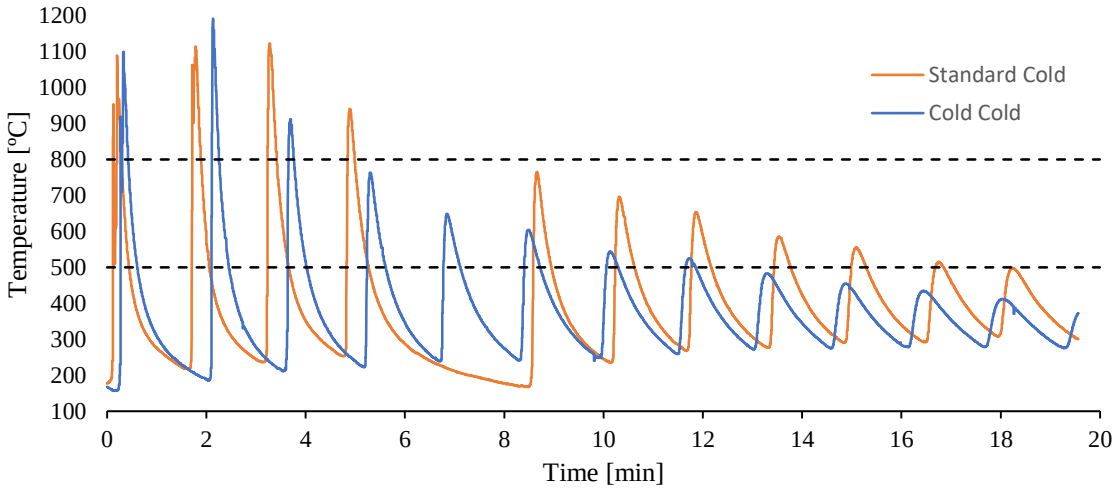

(a)

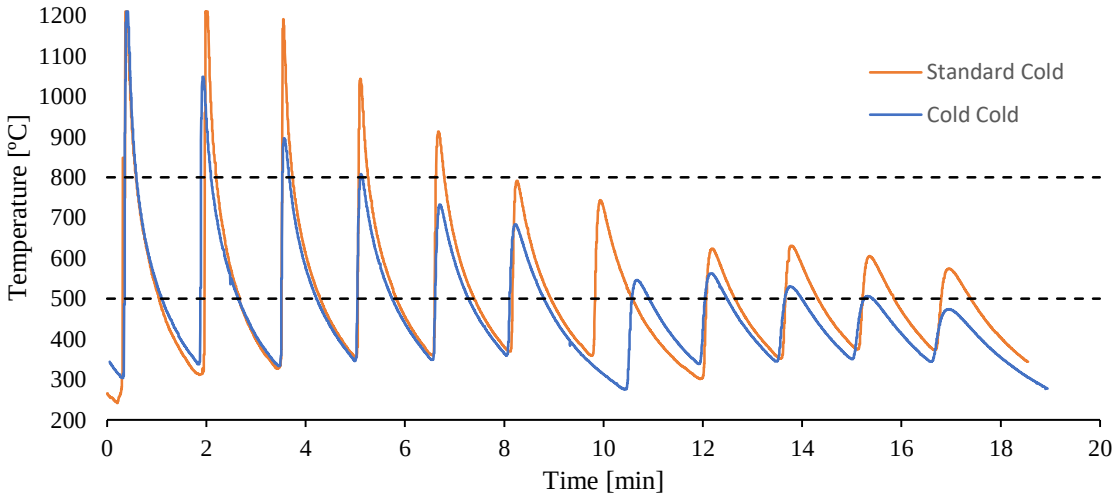

(b)

Figure 4.7: Thermal cycles for samples SC-S and CC-S in: (a) layer 5, (b) layer 15.

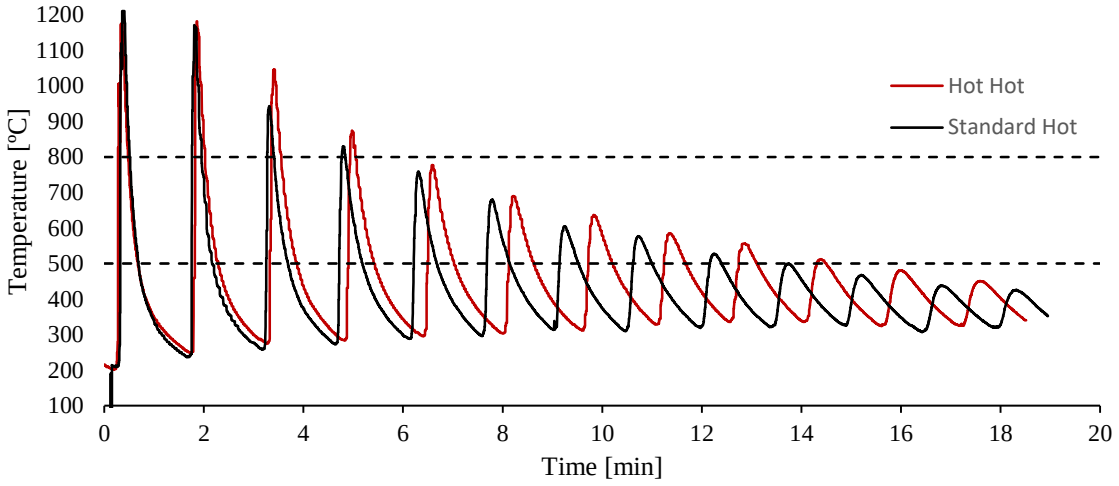

(a)

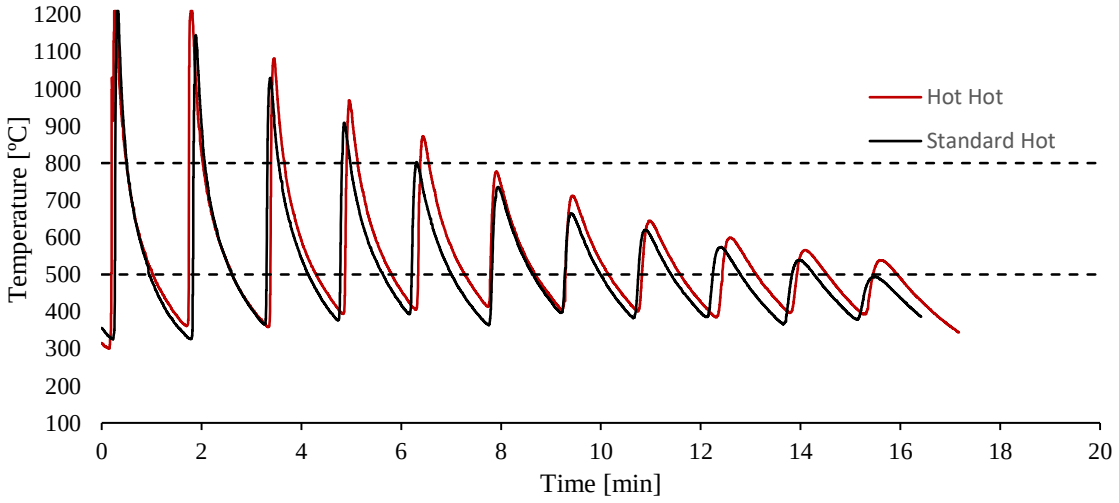

(b)

Figure 4.8: Thermal cycles for samples SH-S and HH-S in: (a) layer 5, (b) layer 15.

Cooling rates for tracking points above were estimated by calculating the temperature difference between each peak and the first temperature value under 500 ºC which was then divided by the corresponding time interval. Data is shown in Figure 4.9.

All the cooling rates drop at an increasingly slower rate when we get further away from the welding pool as expected given the lower amount of energy that reaches the layer where the tracking point is. A significant difference is also noticed between the cooling rates of the first point for both graphics, which shows how with the increase of heat accumulation during depositions, heat dissipation decreases.

By comparing the cooling rates for different samples we can see that samples which were made using the hot exchanger display no noticeable differences and have very similar cooling rates as was expected given that the same was observed for thermal cycles (Figure 4.8). As for samples made using the cold exchanger, only the first measurement made for sample CC-S in layer 5 revealed a slightly higher cooling rate (approximately + 2 ºC/s) when compared to sample SC-S, all the other points show that using cold argon through the cooling exchanger a slower cooling rate was obtained. This in a consequence of the lower energy introduced in the system in each pass as shown in Figure 4.7.

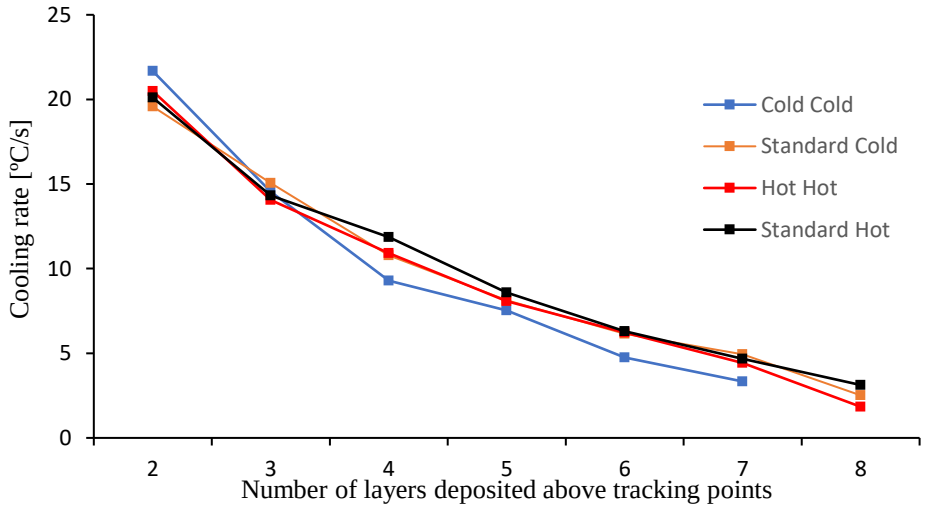

(a)

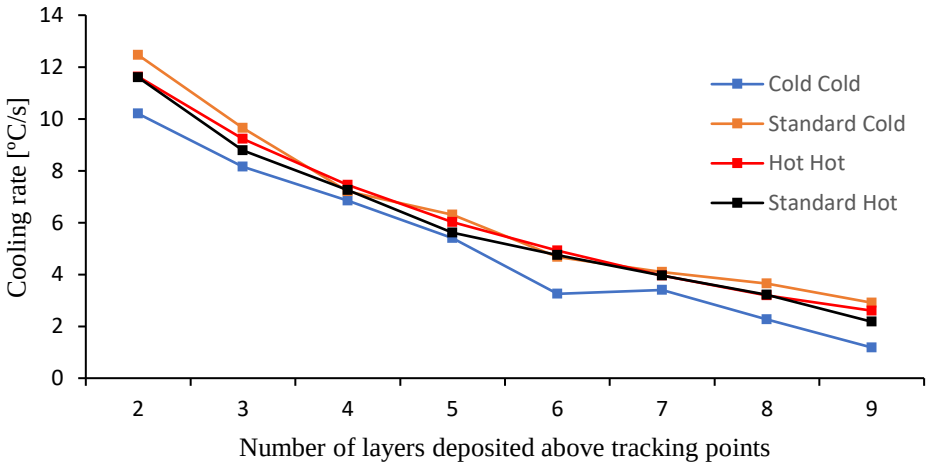

(b)

Figure 4.9: Cooling rates for samples CC-S, SC-S, SH-S and HH-S at: (a) layer 5, (b) layer 15.

Pictures of the building process were also extracted from the thermography videos allowing to measure the temperature of the cooling exchanger with and without cooling turned on. As shown in Figure 4.10, the temperature of cooling exchanger in the region closest to the weld pool was at 171.5 ºC without cooling turned on and at 60.2 ºC with cooling on. This represented a difference of 111.3 ºC.

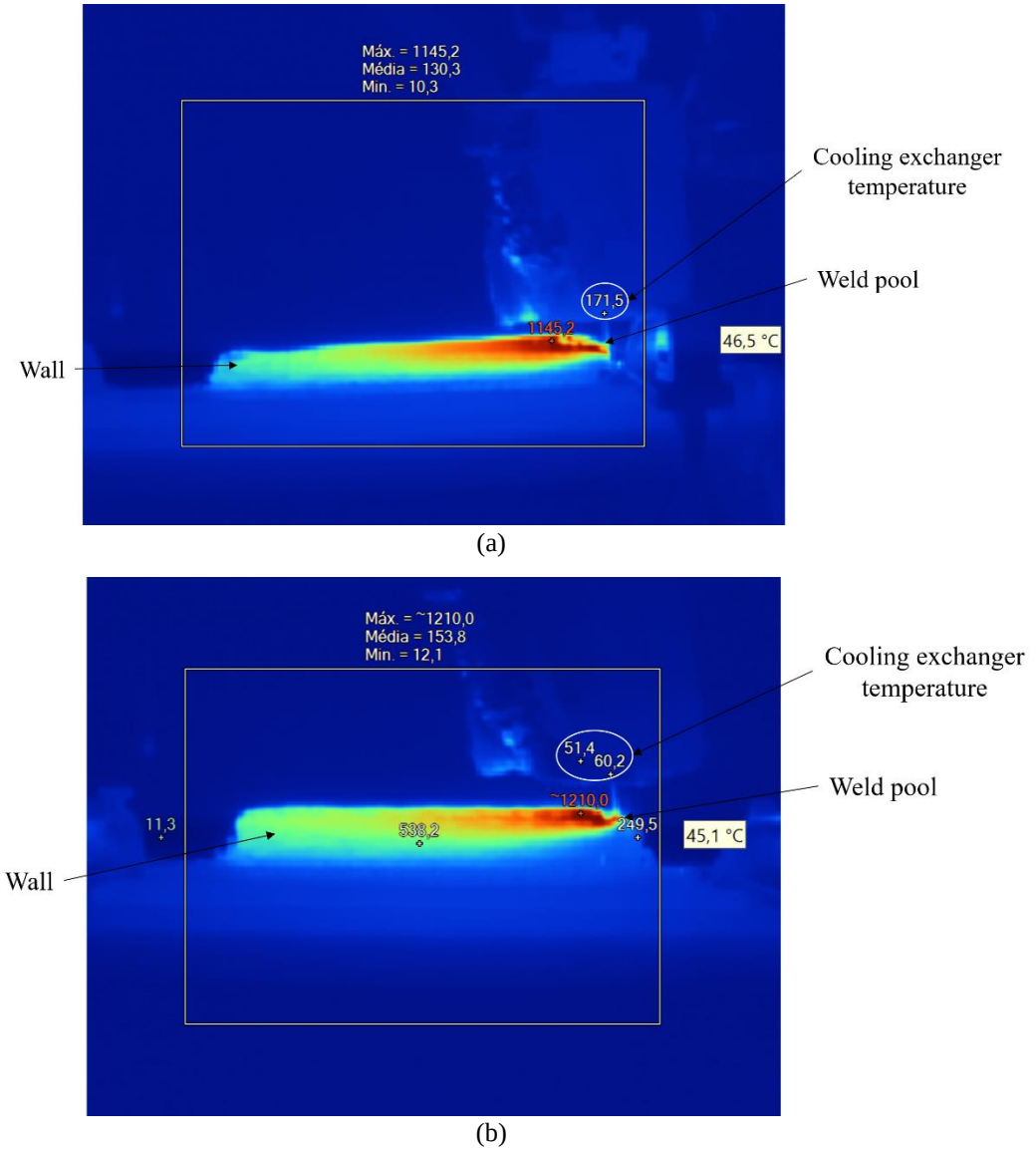

Figure 4.10: Thermography frames captured during wall buildup for samples: (a) SC, (b) CC.

4.3.2 Microhardness

Microhardness results for 316L depositions are displayed in Figure 4.11 but results for samples SC-S (c) and CC-S (d) were ignored and should not be considered since the microhardness testing machine was believed to be faulty at the time of such measurements due to the discrepancy from the previous measurements. For samples SH-S (a) and HH-S (b) the measurements are very similar and show a slight increase in hardness for the first layers which results from the higher cooling rates close to the substrate which acts as a good heat sink. These hardness values are identical to values presented in previous works [16] which suggests that increasing the shielding gas temperature by over 93 ºC has no effect on hardness.

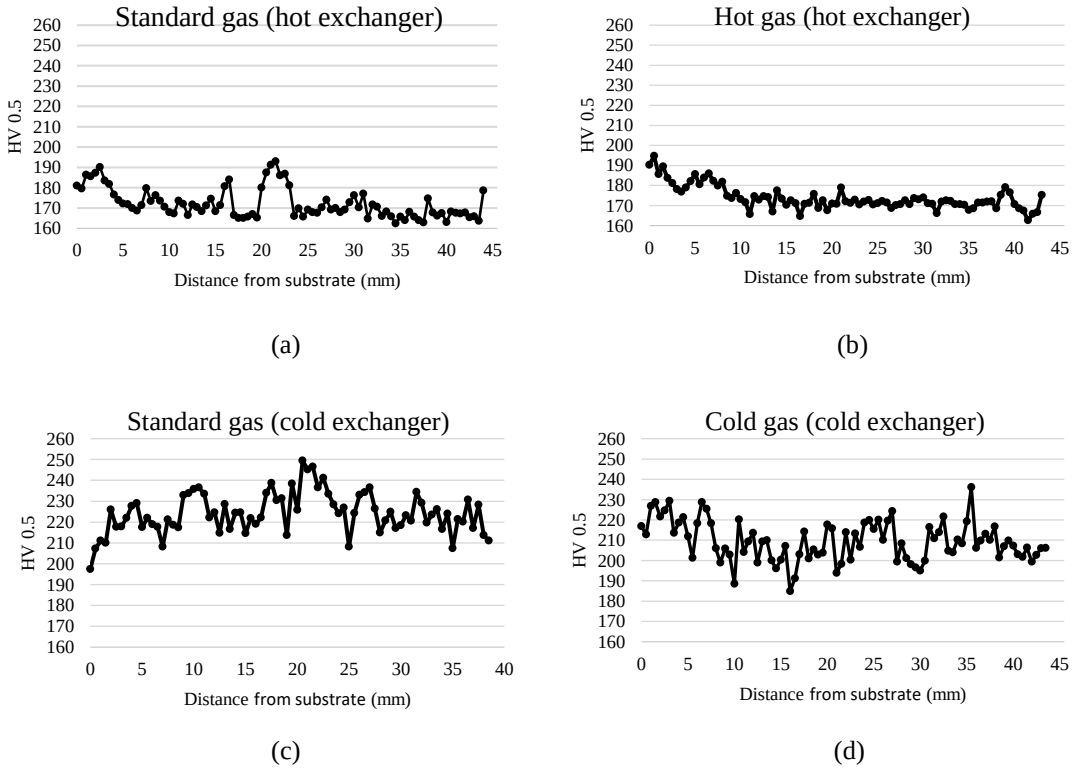

Figure 4.11: Microhardness profile of sample SH-S (a), HH-S (b), SC-S (c) and CC-S (d)

4.3.3 Microstructure

Resulting microstructure for 316L samples is shown in Figure 4.12. Cellular structures can be observed close to the fusion zone (FZ) which then develop into columnar structures growing parallel to the heat flow direction. The primary dendrite arm spacing (PDAS) was measured using *Adobe Photoshop CC 2019* for samples CC-S and SC-S, produced with the cooling exchanger, and results are shown in Figure 4.13. An increase of 12%, from 6.8 μm to 7.6 μm was observed from CC-S to SC-S which shows good agreement with geometry and EWW values measured above (Table 4.4). This also suggests that hardness should be higher for samples produced using cold argon given their smaller grain size, but as mentioned above, the microhardness machine was faulty at the time of such measurements and therefore no conclusions could be made.

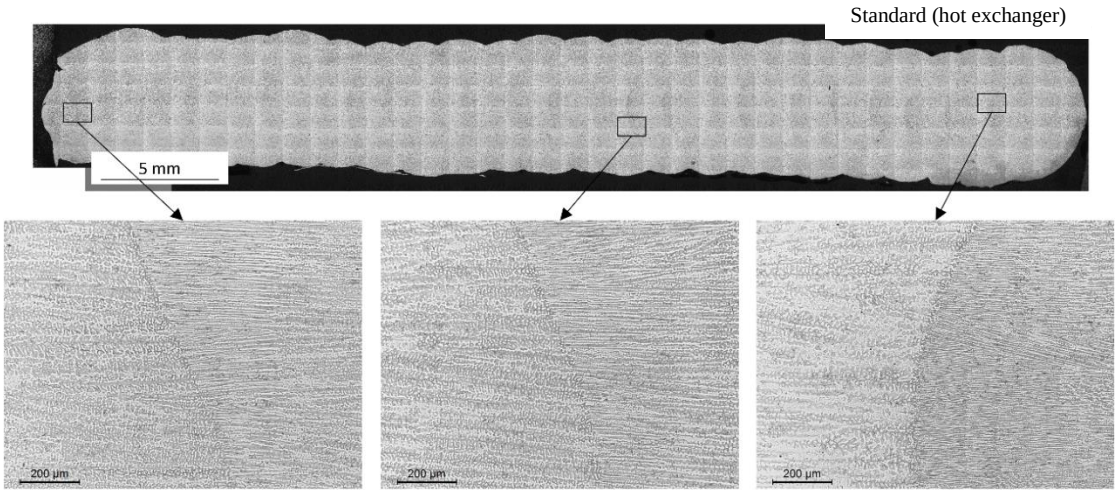

(a)

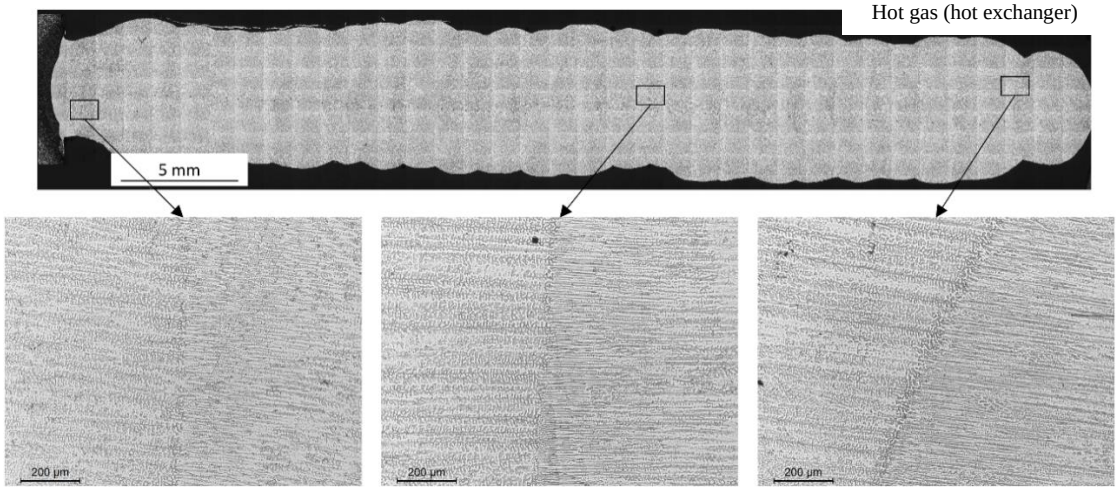

(b)

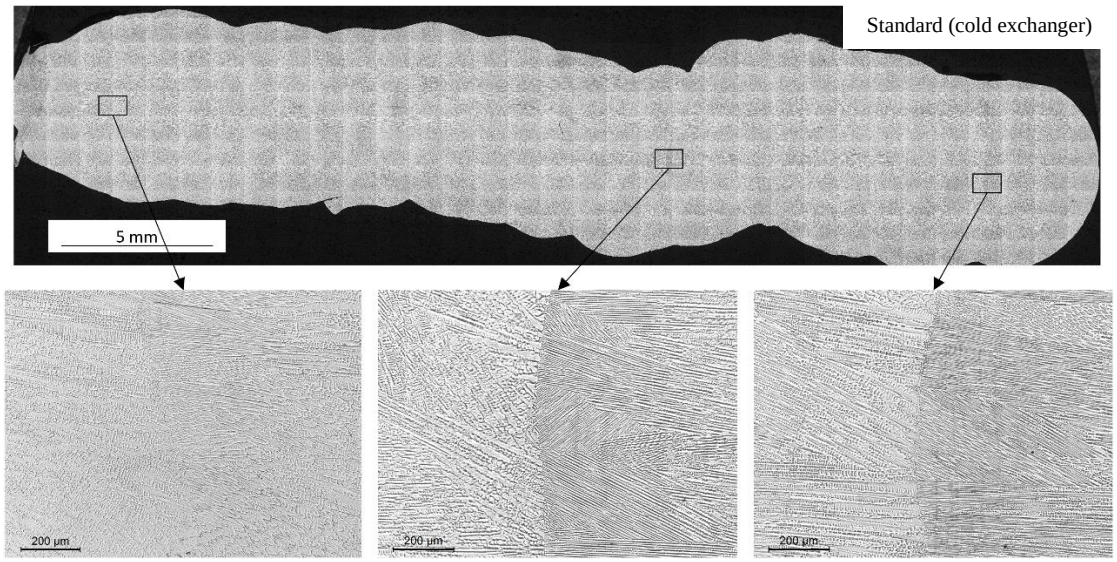

(c)

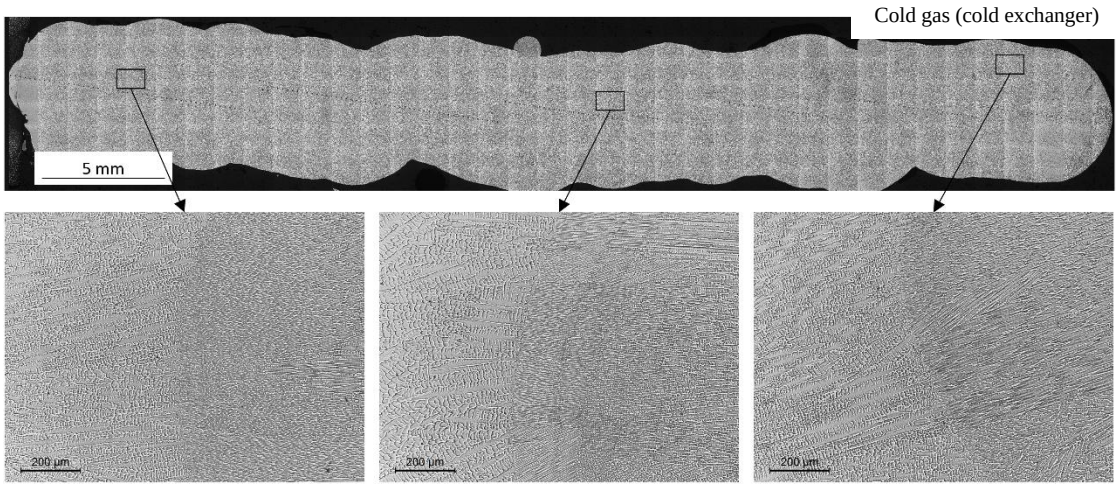

(d)

Figure 4.12: Microstructure of sample SH-S (a), HH-S (b), SC-S (c) and CC-S (d).

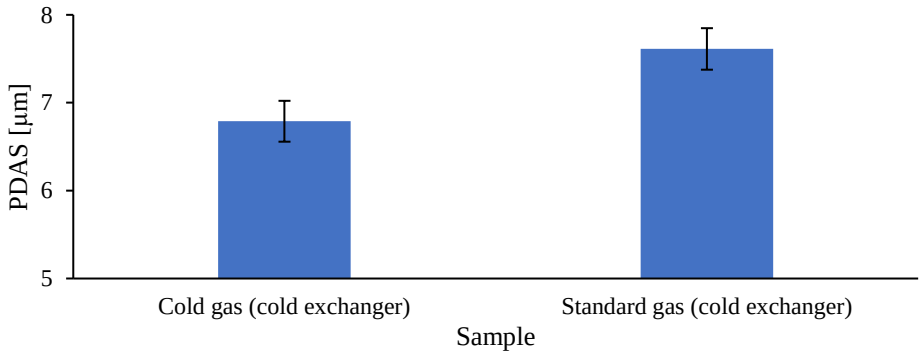

Figure 4.13: Primary dendrite arm spacing (PDAS) for 316L samples.

4.4 Depositions with Inconel 625 superalloy

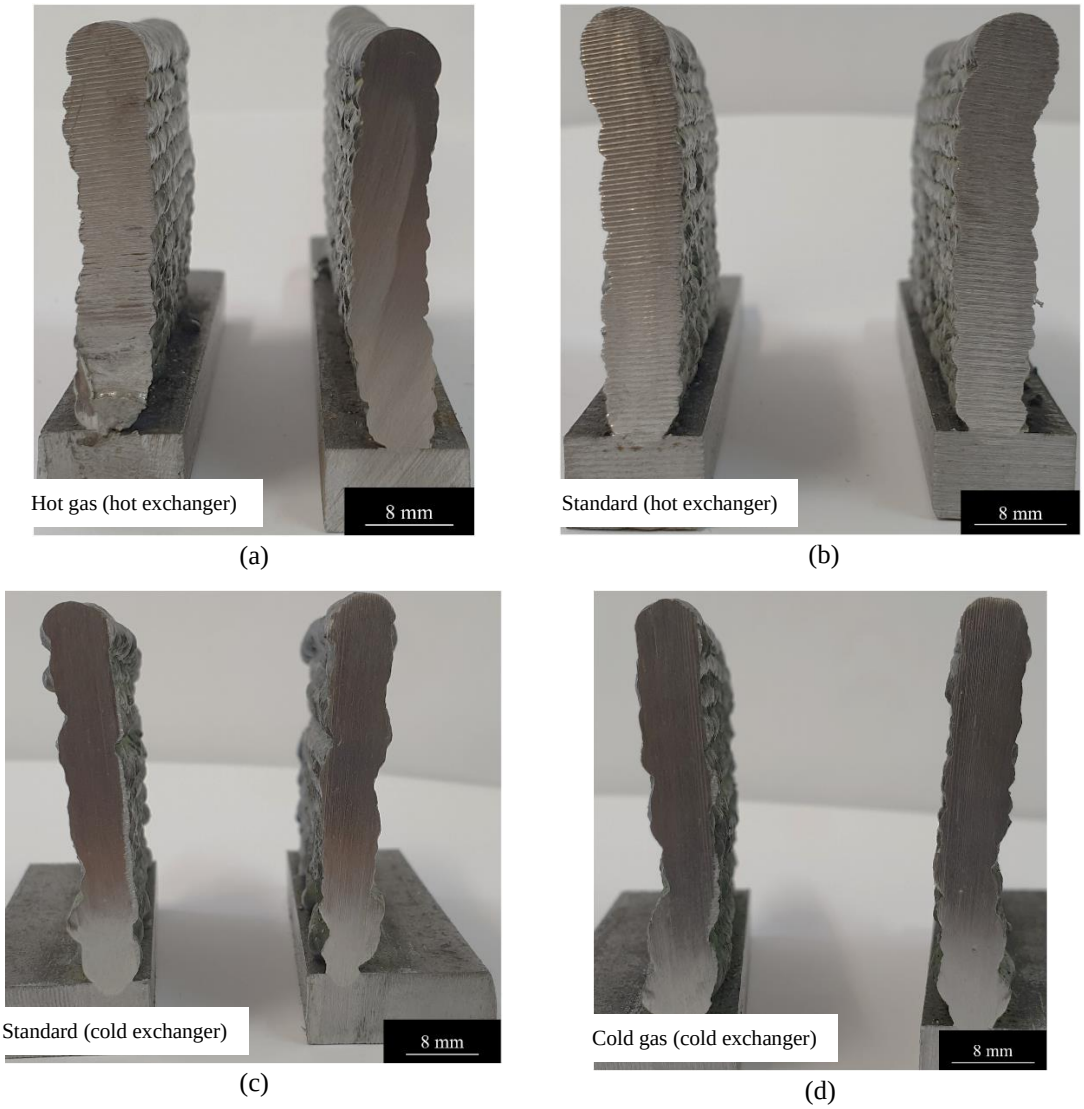

Figure 4.14: Transversal section of sample HH-I (a), SH-I (b), SC-I (c) and CC-I (d).

Walls obtained using Inconel 625 superalloy are shown in Figure 4.14. A clear difference in waviness was noticed between samples produced using the hot shielding gas system and samples produced using the cooling exchanger. Parts produced using the cooling system were very irregular which resulted in relatively small EWW as shown in Table 4.5. Comparing these samples to the ones produced using the hot exchanger, the decrease in EWW ranges from 28.1 % (4.92 – 3.84) to 31.7 % (4.94 – 3.75). This is a result of the increased shielding gas turbulence when using the cooling heat exchanger which can compromise shielding conditions and increase atmosphere contamination [17].

Table 4.5: Average EWW and height of Inconel 625 samples.

Sample	EWW [mm]	Height [mm]
HH-I	4.92	38
SH-I	4.94	39
SC-I	3.75	40
CC-I	3.84	41

4.4.1 Microhardness

Microhardness results for Inconel 625 are shown in Figure 4.15. Samples produced using the hot exchanger displayed very similar hardness values which were within the same values of sample SC-I produced with the cold exchanger. These values are within the expected values [18]. Sample CC-I, produced with the cooling system turned on displayed a significant increase in hardness in the first half of the wall, reaching values up to 278.5 HV which represents an increase of around 30 HV when compared to the rest of the samples. After the first half, hardness values started to decrease and got within the range of other samples.

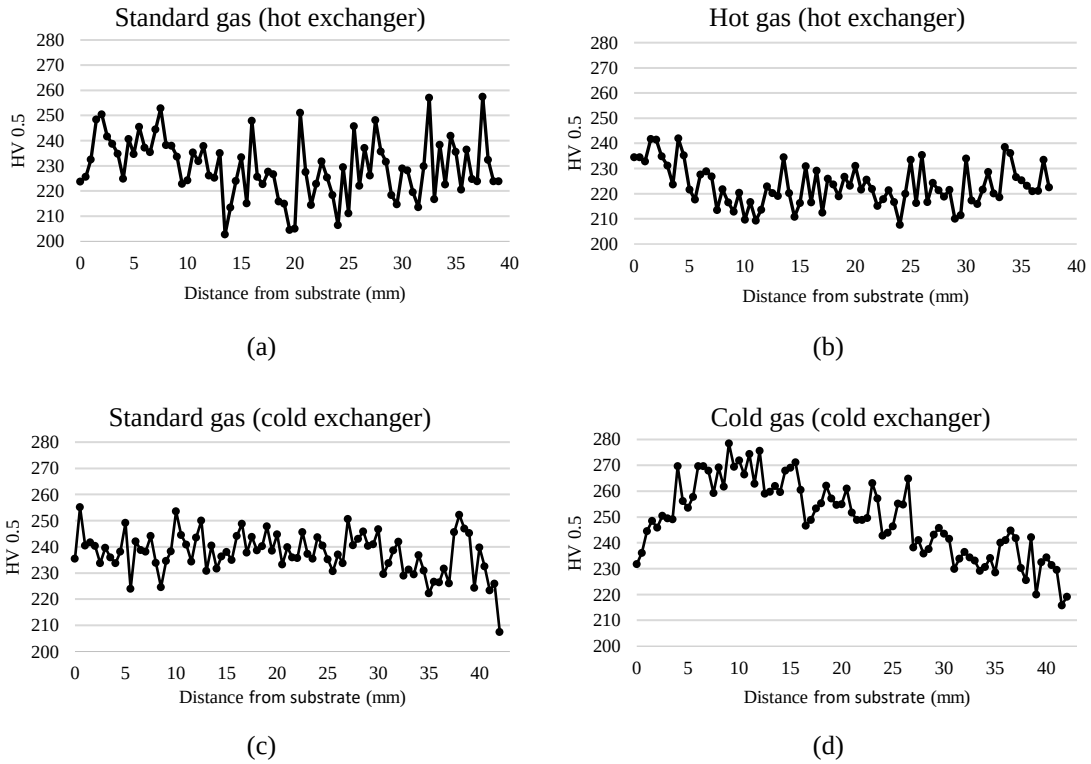

Figure 4.15: Microhardness profile of sample SH-I (a), HH-I (b), SC-I (c) and CC-I (d).

4.4.2 Microstructure

The resulting microstructure for Inconel 625 samples is shown in Figure 4.16. Columnar dendrite was predominant throughout the central region of all samples with some amount of cellular dendritic structure also found.

The PDAS was measured and results are shown in Figure 4.17. Sample CC-I displayed the smallest PDAS with an average of 17.4 μm while the larger arm spacing was measured in sample SC-I with a value of 19.7 μm. This increase of 13% is associated with the difference in energy introduced during depositions and should also explain the differences obtained during microhardness measurements. Samples built using the heating exchanger displayed PDAS very similar (19.2 and 18.4 μm for HH and SH respectively) which shows an agreement with microhardness results.

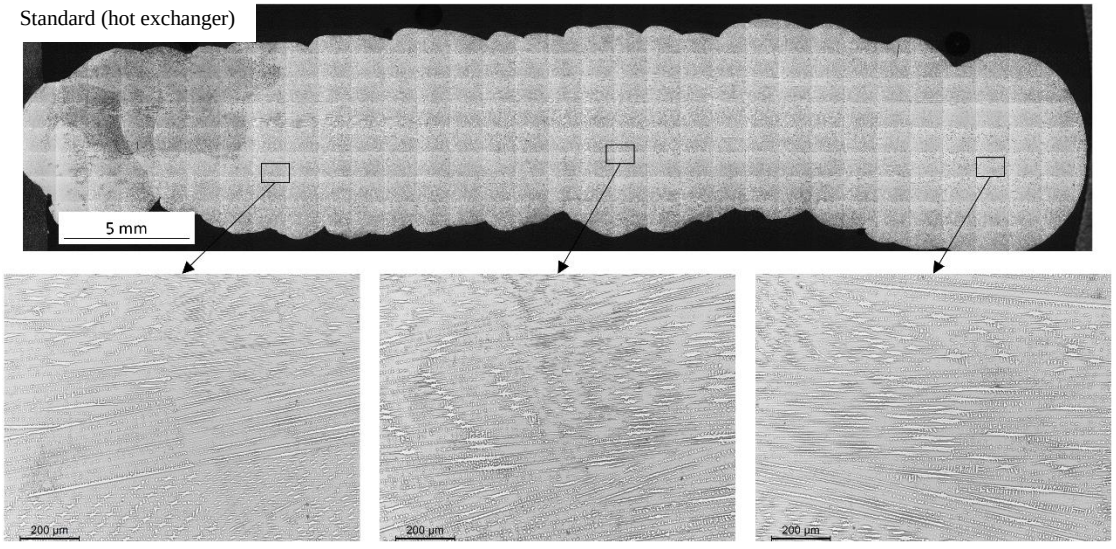

(a)

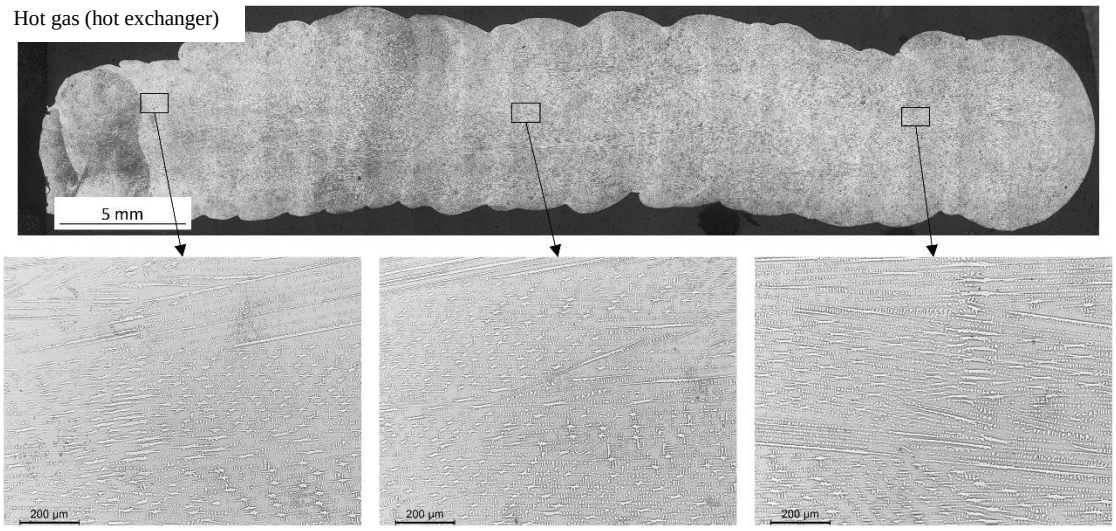

(b)

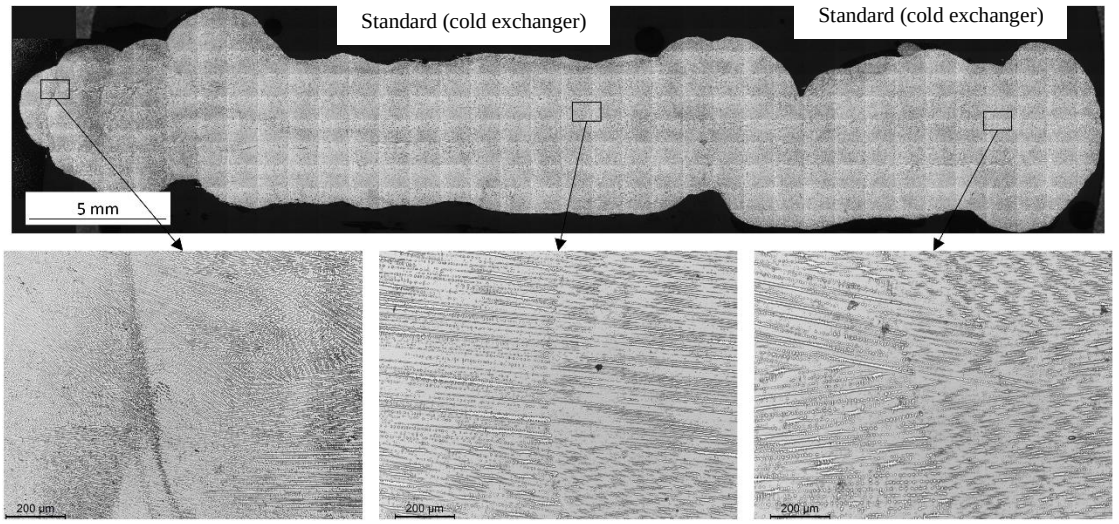

(c)

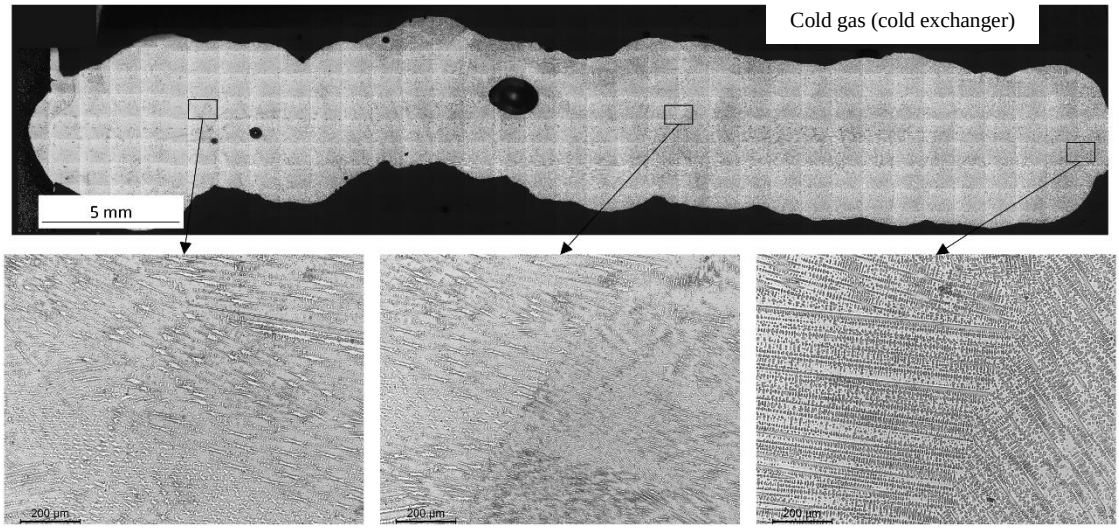

(d)

Figure 4.16: Microstructure of sample SH-I (a), HH-I (b), SC-I (c) and CC-I (d).

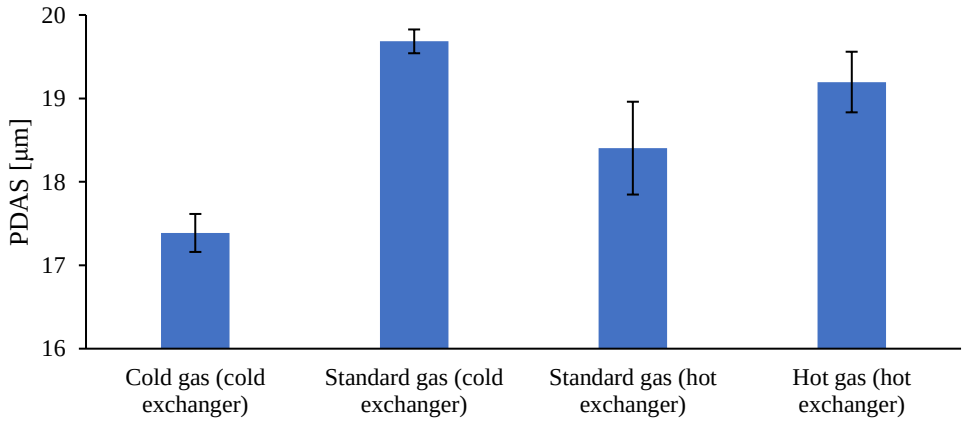

Figure 4.17: Primary dendrite arm spacing (PDAS) for Inconel 625 samples.

4.5 Power comparison

During WAAM processes, the involved power can easily reach values over 2000 W, which translates in a significant amount of heat released. To have a better understanding of how cooling or heating shielding gases during a deposition can affect layer cooling rate, simple approximations were used to determine the thermodynamic energy associated with the temperature variations achieved using the heat exchangers built.

Heat flow can be expressed by equation (4.1), which can be rewritten in terms of mass flow ($\dot{m}$) to obtain a comparable power unit (equation (4.2)).

$$Q = m\, c\, \Delta T \qquad [J] \qquad (4.1)$$

$$\dot{Q} = \dot{m}\, c\, \Delta T \qquad [W] \qquad (4.2)$$

By replacing the mass flow rate and the specific heat values in equation (4.2), 5.95×10^{-4} Kg s^{-1} and 520 J Kg^{-1} K^{-1} respectively, $\dot{Q}$ is given by 0.309 W K^{-1}. Using the heating exchanger, a temperature over 93ºC was achieved, which represents a ΔT of approximately 70 K. This heat exchanger was therefore able to produce a heating power of approximately 21.64 W. Using the cooling heat exchanger, a temperature close to 0ºC was achieved and maintained during depositions. This represents a temperature variation, ΔT, of approximately 25 K, which corresponded to an approximate cooling power of at least 7.73 W.

Both values are not significant when compared to the electric power involved in WAAM which is over 100 times higher and explains the lack of differences between samples produced using the hot exchanger. As for the cooling exchanger, despite having and even lower power, the significant volume of metal kept at low temperatures during depositions served as an additional heat sink which should explain the differences observed in microhardness for Inconel 625 samples. The opposite was also true and should explain results obtained for sample SC-S, produced with the cooling heat exchanger and cooling turned off. Instead of a heat sink, the heat exchanger acted as a heat accumulator reducing heat exchanges between the weld pool and the surrounding atmosphere which resulted in a bead with reduced height and increased width.

5 Conclusions and future work

A system capable of controlling the cooling rate during WAAM without interfering with the shielding gas was developed during this study. For this purpose, two different heat exchangers were built, one to heat and another to cool the shielding gas and the following can be concluded:

1. Regarding the developed equipment:
    - The heating exchanger successfully heated argon to a temperature of 92.66 ºC taking only one minute to reach 90 ºC.
    - The cooling heat exchanger was able to cool down the shielding gas to -2.28 ºC but took almost 7 minutes. The nozzle was cooled down to -8.6 ºC within the same time frame.
    - Using the cooling exchanger, the shielding gas flow suffered from higher turbulence which increased atmosphere contamination and affected wall waviness [17]. This happened due to the absence of a diffuser within the system.
    - The cooling heat exchanger was able to maintain a temperature lower than 60.2 ºC during depositions with the cooling turned on. Without cooling the temperature rose at 111.3 ºC reaching 171.5 ºC.
    - Less energy was introduced into the system using cold argon due to the cooling exchanger acting as a heat sink, while more energy was introduced using ambient argon because the exchanger acted as a heat accumulator.
2. Regarding samples manufactured with 316L stainless steel:
    - Using the cold exchanger with ambient temperature argon (25 ºC) resulted in the largest EWW measurement of 5.2 mm and the smallest height of 38 mm while using the cold exchanger with cold gas resulted in the smallest EWW of 4.45 mm and the highest height of 44 mm.
    - By turning the cold system on, PDAS decreased 11.8% (from 7.6 μm to 6.8 μm).

- Hot shielding gas had no effect on hardness when compared to the ambient gas standard sample.

3. Regarding samples manufactured with Inconel 625 superalloy:
    - Parts made using the cold heat exchanger displayed higher waviness which translated in a reduction of the EWW between 28.1 % and 31.7 %.
    - An increase up to 30 HV was measured 10 mm away from the substrate for sample CC-I, built using the cold exchanger with cooling turned on.
    - No differences in hardness were detected between samples using the hot exchanger with both hot and ambient gas temperature, or using the cold exchanger with ambient temperature gas.
    - Using cold argon, a PDAS of 17.4 μm was measured while using ambient argon in the cold exchanger resulted in a PDAS of 19.7 μm.

Results show that varying the temperature of the shielding gas by itself is not enough to significantly influence the microstructure and mechanical properties of WAAM components. The differences obtained were due to the cooling exchanger acting as a heat sink or as a heat accumulator depending on whether the cooling was turned on or off which is similar to thermoelectric cooling as shown by Li et al. [19].

Nevertheless, outcomes were very distinct when comparing Inconel 625 and 316 SS results and some suggestions for future works are:

- Creating a version of the cooling exchanger able of also heating the shielding gas.
- Testing the cooling exchanger with different materials.
- Doing more mechanical tests such as the uniaxial tensile test and Charpy tests.
- Creating a version of the cooling exchanger with a larger diameter to increase the heat sink/accumulator effect.

References

[1] S. W. Williams, F. Martina, A. C. Addison, J. Ding, G. Pardal, and P. Colegrove, "Wire + Arc Additive Manufacturing," *Mater. Sci. Technol.*, vol. 32, no. 7, pp. 641–647, May 2016.

[2] B. Wu *et al.*, "A review of the wire arc additive manufacturing of metals: properties, defects and quality improvement," *J. Manuf. Process.*, vol. 35, pp. 127–139, Oct. 2018.

[3] J. Bai, H. L. Ding, J. L. Gu, X. S. Wang, and H. Qiu, "Porosity evolution in additively manufactured aluminium alloy during high temperature exposure," *IOP Conf. Ser. Mater. Sci. Eng.*, vol. 167, p. 012045, Jan. 2017.

[4] J. Gu *et al.*, "The strengthening effect of inter-layer cold working and post-deposition heat treatment on the additively manufactured Al–6.3Cu alloy," *Mater. Sci. Eng. A*, vol. 651, pp. 18–26, Jan. 2016.

[5] A. R. McAndrew *et al.*, "Interpass rolling of Ti-6Al-4V wire + arc additively manufactured features for microstructural refinement," *Addit. Manuf.*, vol. 21, pp. 340–349, May 2018.

[6] N. Lippitz, S. Maudarbocus, and J. Rösler, "The influence of cold rolling on the pore morphology and flow resistivity of porous aluminum," *Sixth Int. Conf. Porous Media Its Appl. Sci. Eng. Ind.*, Jul. 2016.

[7] B. Wu, Z. Pan, D. Ding, D. Cuiuri, H. Li, and Z. Fei, "The effects of forced interpass cooling on the material properties of wire arc additively manufactured Ti6Al4V alloy," *J. Mater. Process. Technol.*, vol. 258, pp. 97–105, Aug. 2018.

[8] O. K. von Goldbeck, "Iron—Carbon Fe—C," in *IRON—Binary Phase Diagrams*, O. K. von Goldbeck, Ed. Berlin, Heidelberg: Springer, 1982, pp. 23–26.

[9] G. Krauss, "Martensite in steel: strength and structure," *Mater. Sci. Eng. A*, vol. 273–275, pp. 40–57, Dec. 1999.

[10] "Practical Maintenance » Blog Archive » I-T Diagram and Cooling Curves." [Online]. Available: https://practicalmaintenance.net/?p=1345. [Accessed: 16-Feb-2019].

[11] M. Umemoto, Z. H. Guo, and I. Tamura, "Effect of cooling rate on grain size of ferrite in a carbon steel," *Mater. Sci. Technol.*, vol. 3, no. 4, pp. 249–255, Apr. 1987.

[12] X. Di, S. Ji, F. Cheng, D. Wang, and J. Cao, "Effect of cooling rate on microstructure, inclusions and mechanical properties of weld metal in simulated local dry underwater welding," *Mater. Des.*, vol. 88, pp. 505–513, Dec. 2015.

[13] D. Yang, G. Wang, and G. Zhang, "Thermal analysis for single-pass multi-layer GMAW based additive manufacturing using infrared thermography," *J. Mater. Process. Technol.*, vol. 244, pp. 215–224, Jun. 2017.

[14] "Overall Heat Transfer Coefficient Table Charts and Equation | Engineers Edge | www.engineersedge.com." [Online]. Available: https://www.engineersedge.com/thermodynamics/overall_heat_transfer-table.htm. [Accessed: 20-Aug-2019].

[15] Q. Wu, Z. Ma, G. Chen, C. Liu, D. Ma, and S. Ma, "Obtaining fine microstructure and unsupported overhangs by low heat input pulse arc additive manufacturing," *J. Manuf. Process.*, vol. 27, pp. 198–206, Jun. 2017.

[16] L. Wang, J. Xue, and Q. Wang, "Correlation between arc mode, microstructure, and mechanical properties during wire arc additive manufacturing of 316L stainless steel," *Mater. Sci. Eng. A*, vol. 751, pp. 183–190, Mar. 2019.

[17] J. Ding, P. Colegrove, F. Martina, S. Williams, R. Wiktorowicz, and M. R. Palt, "Development of a laminar flow local shielding device for wire+arc additive manufacture," *J. Mater. Process. Technol.*, vol. 226, pp. 99–105, Dec. 2015.

[18] W. Yangfan, C. Xizhang, and S. Chuanchu, "Microstructure and mechanical properties of Inconel 625 fabricated by wire-arc additive manufacturing," *Surf. Coat. Technol.*, vol. 374, pp. 116–123, Sep. 2019.

[19] F. Li, S. Chen, J. Shi, Y. Zhao, and H. Tian, "Thermoelectric Cooling-Aided Bead Geometry Regulation in Wire and Arc-Based Additive Manufacturing of Thin-Walled Structures," *Appl. Sci. Switz.*, vol. 8, Jan. 2018.